Causes of interannual variability over the southern hemispheric tropospheric ozone maximum

Junhua Liu[1,2], Jose M. Rodriguez[2], Stephen D. Steenrod[1,2], Anne R. Douglass[2], Jennifer A. Logan[3], Mark A Olsen[2,4], Krzysztof Wargan[2,5], Jerald R. Ziemke[2,4]

[1] Universities Space Research Association (USRA), GESTAR, Columbia, MD, USA

[2] NASA Goddard Space Flight Center, Greenbelt, Maryland, USA

[3] School of Engineering and Applied Sciences, Harvard University, Cambridge, MA, USA

[4] Morgan State University, Baltimore, Maryland, USA

[5] Science Systems and Applications, Inc., Lanham, MD, USA

Correspondence to: Junhua Liu (junhua.liu@nasa.gov)

Abstract.

We examine the relative contribution of processes controlling the interannual variability (IAV) of tropospheric ozone over four sub-regions of the southern hemispheric tropospheric ozone maximum (SHTOM) over a twenty-year period. Our study is based on hindcast simulations from the National Aeronautics and Space Administration Global Modeling Initiative – Chemistry transport model (NASA GMI-CTM) of tropospheric and stratospheric chemistry, driven by assimilated Modern Era Retrospective-Analysis for Research and Applications (MERRA) meteorological fields. Our analysis shows that over SHTOM region, the IAV of the stratospheric contribution is the most important factor driving the IAV of upper tropospheric ozone (270 hPa), where ozone has a strong radiative effect. Over the south Atlantic region, the contribution from surface emissions to the IAV of ozone exceeds that from stratospheric input at and below 430 hPa. Over the south Indian Ocean, the IAV of stratospheric ozone makes the largest contribution to the IAV of ozone with little or no influence from surface emissions at 270 hPa and 430 hPa in austral winter. Over the tropical south Atlantic region, the contribution from IAV of stratospheric input dominates in austral winter at 270 hPa and drops to less than half but is still significant at 430 hPa. Emission contributions are not significant at these two levels. The IAV of lightning over this region also contributes to the IAV of ozone in September and December. Over the tropical southeastern Pacific, the contribution of the IAV of stratospheric input is significant at 270 hPa and 430 hPa in austral winter, and emissions have little influence.

1 Introduction

Tropospheric ozone plays a critical role in controlling the oxidative capacity of the troposphere through its photolysis in the presence of water vapor, generating hydroxyl radical (OH), the main atmospheric oxidant (e.g., Logan et al., 1981). It contributes to smog and is harmful to human and ecosystem health near the surface. It acts as a greenhouse gas especially in the upper troposphere (Lacis et al., 1990) and affects the radiative forcing of the climate system. Tropospheric ozone is produced by photochemical oxidation of CO and volatile organic compounds (VOCs) in the presence

of nitrogen oxides (NO_X) (e.g., Logan et al., 1981). Downward transport of ozone from the stratosphere is also an important source of tropospheric ozone (e.g., Danielsen, 1968; Stohl et al., 2003). Deep convection and long-range transport of ozone and its precursors also modulate the tropospheric O_3 distributions (e.g., Chandra et al., 2009; Oman et al., 2011).

Our study is motivated by the presence of tropospheric ozone maximum over tropical and subtropical southern hemisphere as seen both in model simulations and GMAO assimilated ozone product derived from OMI/MLS satellite measurements (Figure 1). Although in the southern hemisphere tropospheric air is relatively "clean" and less polluted compared with the Northern Hemisphere, this tropospheric ozone column maximum reaches as high as 35DU and is comparable to the typical northern mid-latitude values of 30DU. The elevated tropospheric ozone column is centered over the south Atlantic from the equator to 30°S, and is part of the well-known tropical wave-one pattern first noted in observations made by the Nimbus 7 Total Ozone Mapping Spectrometer (TOMS) (e.g., Fishman et al., 1990; Ziemke et al., 1996). This ozone maximum extends westward to South America and the tropical southeastern Pacific, southeastward to southern Africa, south Indian Ocean along the latitude band of 30°S-45°S, and is a dominant global feature (Thompson et al., 2003; Sauvage et al., 2007). This elevated ozone region exists year-around, with a seasonal maximum in August - October, and a seasonal minimum in April - May.

This study provides an examination of the relative contributions of the factors that control the interannual variations of the southern hemisphere tropospheric ozone maximum over a twenty-year period. Prior studies have examined the processes that produce the southern hemisphere tropospheric ozone maximum (SHTOM), but consider only short periods or are limited in spatial scale. These studies concluded that horizontal and vertical transport of ozone precursors from regions of biomass burning (e.g., Jacob et al., 1996; Thompson et al., 1996; Pickering et al., 1996; Jenkins and Ryu, 2004b; Sauvage et al., 2006; Jourdain et al., 2007; Thouret et al., 2009), lightning NO_X (Martin et al., 2002; Jenkins and Ryu, 2004a; Kim et al., 2013; Tocquer et al., 2015) and stratospheric intrusions (Weller et al., 1996) all contribute to this tropospheric ozone column maximum. However, changes of the relative contributions of these factors to tropospheric

ozone on inter-annual time scale over this region have not been examined in detail. Studies considering tropospheric ozone interannual variability have not focused on the SHTOM region. Hess and Mahowald (2009) used a CTM to quantify relative interannual variability in global model ozone in hindcast simulations with constant emissions and prescribed stratospheric ozone. The CTM was driven by two sets of meteorological fields: a) the National Center for Environmental Prediction/National Center for Atmospheric Research reanalysis; b) from a simulation using the Community Atmosphere Model (CAM-3) forced with observed sea surface temperatures. Their study found that relative IAV of ozone at 500 hPa shows the maximum between the Equator and 30S in June-July-August (JJA) and December-January-February (DJF). Zeng and Pyle (2005) used a climate/chemistry model to evaluate the ENSO effects on the interannual variability of tropospheric ozone. Their study concludes that STE variation induced by ENSO is one important factor driving the IAV of the global mean of tropospheric ozone. Voulgarakis et al. (2010) examined the drivers of interannual variability of the global tropospheric ozone using the p-TOMCAT tropospheric chemistry transport model (CTM). Their study shows that changing transport including the STE is important in determining the IAV of tropospheric ozone. Voulgarakis et al. (2011) demonstrated that increases in the amounts of stratospheric ozone entering the troposphere following El Niño events are mainly driven by changes in the STE. The influence of emissions is confined to areas of intense burning on the interannual timescale. Murray et al. (2013) examined the effects of lightning on the IAV in the tropical tropospheric ozone column based on the GEOS-Chem CTM with IAV in tropical lightning constrained by satellite observations from Lightning Imaging Sensors (LIS). Their study finds that lightning plays an important role in driving the IAV of tropical tropospheric ozone column, especially over East Africa, central Brazil, and in continental outflow in the eastern Pacific and the Atlantic, but their model does not reproduce the IAV in TCO except in East Africa and central Brazil. Liu et al. (2016) analyzed simulations from a global chemistry and transport model to show that the IAV in the stratospheric contribution significantly affects the IAV of upper tropospheric ozone at the SHADOZ station over Reunion (21°S). In this study, we focus on the SHTOM region and quantify the relative contributions of several factors to the tropospheric ozone

interannual variability during the past twenty years. We examine the horizontal and vertical variations of these contributions by separating the SHTOM into four subregions and comparing their IAVs at two selected levels (270 hPa and 430 hPa). This analysis distinguishes between anthropogenic and natural sources on the IAV of the tropospheric ozone and their contributions to the radiative forcing changes.

In this study, we use a global chemistry transport model to identify the processes impacting observed interannual variability of the tropospheric ozone column maximum in southern hemisphere. We examine the model sensitivity of tropospheric ozone to different ozone sources through the use of multiple linear regression. We include stratospheric input and emissions as two major predictor variables in our regression. We include the lightning NO_X as the third factor in our regression model over the tropical south Atlantic region, where ozone is sensitive to the IAV of lightning NO_X as found in Murray et al (2013). In our multiple linear regression, a regression coefficient that is significantly different from zero at the 95% confidence level implies that the corresponding process contributes significantly to the variation of simulated ozone. To estimate the variance explained by each predictor, we first calculate the sequential sums of squares over ordering of predictors (see supplementary materials). The sequential of squares depends on the predictors already in the model; we therefore do the calculation for every possible order in which predictors can enter the model. We then average all the sequential sums of squares to yield an adjusted sum of squares (Kruskal, 1987; Chevan and Sutherland, 1991; Groemping, 2007). This method accounts for the likely possibility that the two predictors are not orthogonal. We use the adjusted sum of squares to quantify the relative contributions of each predictor to the interannual variability of tropospheric ozone. Our study focuses on austral winter season when the subtropical jet related stratosphere - troposphere exchange reaches the seasonal maximum (Karoly et al., 1998; Bals-Elsholz et al., 2001; Nakamura and Shimpo, 2004). Southern hemisphere biomass burning (e.g., Liu et al., 2010; 2013) also reaches the maximum during this season.

Section 2 briefly describes the model and simulations, including the standard chemistry simulation, the stratospheric O_3 tracer simulation, and the tagged CO simulation. It also describes GEOS-5 ozone assimilation, as the assimilated fields are used to evaluate model performance over the southern hemisphere extra-tropics and tropics as discussed

in the first part of Section 3. The second part of Section 3 presents a diagnostic study of controlling factors, including stratosphere input, surface emissions and lightning, on the tropospheric ozone IAV relying on a series of hindcast simulations from 1992 to 2011. Section 4 is a summary and conclusion.

2 Model and Data

2.1 Model

We used the Global Modeling Initiative chemical transport model (GMI-CTM) (Duncan et al., 2007; Strahan et al., 2007), driven by MERRA reanalysis meteorology (Rienecker et al., 2011, http://gmao.gsfc.nasa.gov/research/merra/). The native resolution of the MERRA field is $0.67° \times 0.5°$ with 72 vertical levels; we regrid it to 2°x2.5° horizontal grid for input to the GMI-CTM simulations in this study.

The chemical mechanism used in GMI-CTM represents stratospheric and tropospheric chemistry with offline aerosols input from GOCART model simulations (Chin et al., 2002). The GMI-CTM hindcast simulation has been used and compared to observations in many recent studies. Strahan et al. (2013) showed excellent agreement between simulated and MLS ozone profiles in the Arctic lower stratosphere. Liu et al. (2016) shows the GMI-CTM hindcast and ozonesonde agree very well on the annual cycles and IAV over Reunion from lower troposphere to the upper troposphere. Strode et al. (2015) shows that the GMI-CTM hindcast reproduces the seasonal cycle and IAV of observed surface ozone over United States from Environmental Protection Agency (EPA)'s Clean Air Status and Trends Network (CASTNET).

The GMI-CTM standard simulation (labeled as Hindcast-VE) used in this study for 1992-2011 includes monthly and inter-annually varying emissions with anthropogenic, biomass burning, and biogenic sources. Anthropogenic emissions are based on the EDGAR 3.2 Inventory (Olivier et al., 2005), overwritten with available regional inventories for North America, Europe, Asia and Mexico. More details are given in Strode et al. (2015). Biomass burning emissions are from the Global Fire Emission Database, GFED3 (van der Werf et al., 2010). Emission before 1997 are obtained from GFED3 emission climatology averaged for 2001 to 2009 applied with regional-scale IAV, which was

derived from satellite information on fire activity (ATSR) and/or aerosol optical depths from the Total Ozone Mapping Spectrometer (TOMS) by Duncan et al. (2003). Biogenic emissions of isoprene and monoterpenes follow the latest version of the MEGAN algorithm (Guenther et al., 2006). Besides the standard simulation, we carry out a control run for 1991-2011 by repeating the anthropogenic and biomass emissions for 2000. The comparison between the control and standard simulation removes the possible impact of IAV in meteorology and allows us to quantify effects of emission IAV on ozone IAV.

In our GMI-CTM, the lightning parameterization follows the scheme described by Allen et al (2010). The regional lightning NO_X emission, calculated online by coupling to the deep convective transport in the model, varies from year to year. The global total of NO_X from lightning is fixed at 5.0 TgN/yr.

Methane mixing ratios are specified in the two lowest model levels, using time dependent zonal means from National Oceanic and Atmospheric Administration / Global Monitoring Division (NOAA/GMD). Other long-lived source gases important in the stratosphere, such as N_2O, CFCs, halocarbons are prescribed at the two lowest model levels following the A2 scenario by (WMO, 2014). Stratospheric aerosol distributions/trends are from International Global Atmospheric Chemistry/Stratospheric Processes And their Role in Climate (IGAC/SPARC) and have IAV (Eyring et al., 2013).

The model includes a stratospheric O_3 tracer ($StratO_3$). The $StratO_3$ is defined relative to a dynamically varying tropopause tracer (e90) (Prather et al., 2011). The e90 tracer is set to a uniform mixing ratio (100 ppb) at the surface with 90 days e-folding lifetime. In our simulation, the e90 tropopause value is 75 ppb. The $StratO_3$ tracer is set equal to O_3 in the stratosphere and is removed in the troposphere with the same loss frequency (chemistry and deposition) archived from daily output of the standard chemistry model simulation with yearly-varied emission in this study. Using the $StratO_3$ tracer allows quantification of O_3 of stratospheric origin in the troposphere at a given location and time. This approach has also been adopted in the high resolution GFDL AM3 model (Lin et al., 2012).

In this study, we also conducted a tagged CO simulation to examine the emission sources during the same period as the full chemistry simulation. The tagged CO simulation has

194 horizontal resolution of 1°x1.25°. The primary chemical loss of CO is through reactions
195 with OH radicals, which are archived from the respective standard chemistry simulation
196 with yearly-varied emissions. The chemical production and loss rates of CO in the
197 stratosphere were archived from the respective standard chemistry simulations.

198 **2.2 GMAO GEOS-5 Ozone Assimilation**

199 We used assimilated tropospheric ozone to evaluate model performance. This assimilated
200 dataset is produced by ingesting OMI v8.5 total column ozone and MLS v3.3 ozone
201 profiles into a version of the Goddard Earth Observing System, Version 5 (GEOS-5) data
202 assimilation system (Rienecker et al., 2011). No ozonesonde data are used in the
203 assimilation. Wargan et al. (2015) provides details of the GEOS-5.7.2 assimilation
204 system, which for this application is produced with 2° x 2.5° horizontal resolution and
205 with 72 vertical layers between the surface and 0.01 hPa. For the troposphere, the
206 assimilation only applies a dry deposition mechanism at the surface without any chemical
207 production or loss. This algorithm works since the ozone lifetime is much longer than the
208 six-hour analysis time on which the background field is corrected by observations.
209 Ziemke et al. (2014) evaluated the tropospheric ozone profiles derived from three
210 strategies based on OMI and MLS measurements, including this GEOS-5 assimilation,
211 trajectory mapping and direct profile retrieval using residual method, with ozonesonde
212 observations and GMI model simulations. They show that the ozone product (500 hPa to
213 tropopause) from the GEOS-5 assimilation is the most realistic. Wargan et al. (2015) also
214 demonstrate that the ozone between 500 hPa and the tropopause from GEOS-5
215 assimilation is in good agreement with independent observations from ozonesondes. The
216 assimilation applies the OMI averaging kernels in the troposphere, but the weight of OMI
217 kernels decreases sharply below 500 hPa (Personal communication with K. Wargan).
218 Considering that in the lower troposphere there is no direct observational constraint in
219 the analysis, we use ozone mixing ratio at 270 hPa and 430 hPa as well as partial column
220 ozone integrated from 500 hPa to the tropopause from GEOS-5 assimilation as a
221 reference value to evaluate our GMI model simulation. To compare the GEOS-5
222 assimilated tropospheric partial column above 500 hPa with GMI-CTM ozone

simulation, we use the same tropopause as defined by the lower of the 3.5 potential vorticity units (PVU) isosurface and the 380 K isentropic surface.

3 Results

3.1 Temporal and spatial distribution of SHTOM in GMI-CTM and GMAO GEOS-5 assimilated ozone product

Figure 1 shows the spatial pattern of southern hemispheric partial column ozone (from 500 hPa to the tropopause) in four seasons averaged over 2005 to 2011 from the GMAO GEOS-5 assimilated dataset and the GMI-CTM hindcast simulations. To account for a low bias in the GEOS-5 ozone product (Wargan et al., 2015), we added 2.5 DU to the assimilated column in the tropics (0-30°S). The GMI-CTM simulation reproduces the seasonality and spatial distribution of southern hemispheric ozone maximum as shown in GEOS-5 assimilated product with a) the elevated ozone centered over the Atlantic Ocean from the equator to 40°S; b) the ozone maximum extending southeastward to southern Africa and the Indian Ocean in the latitude band of 30°S-45°S; c) the relatively weaker enhancement extending westward to South America and the tropical southeastern Pacific. The ozone maximum is strongest in austral winter-spring and weakest in austral fall. Both GMI-CTM and GEOS-5 assimilation show the very low tropospheric ozone over the western Pacific and the tropical eastern Indian Ocean, where the ozone - poor marine boundary layer air is lifted into the upper troposphere (Folkins et al., 2002; Solomon et al., 2005).

3.2 Subregions of SHTOM

The tropospheric ozone distribution in any region depends on the advection and mixing, its proximity to the polluted area, and descent of ozone-rich air from the stratosphere. We show in Figure 2 the maps of simulated O_3 and $Strat O_3/O_3$ at 430 hPa averaged over 1992 to 2011 in September, when the southern hemisphere biomass burning peaks. The $Strat O_3/O_3$ ratio represents the fraction of tropospheric ozone from the stratosphere and is used to identify the regions with distinct stratospheric input. Differences in the spatial

patterns of the maximum/minimum in ozone mixing ratio and $StratO_3/O_3$ ratio identifies regions where ozone is affected by factors other than the stratospheric input.

The region with minimum stratospheric ozone contribution occurs along the equator. In the tropics, the southward extension of regions with minimum stratospheric ozone contribution shows zonal variation, reaching 5°S to 10°S over tropical eastern Pacific and tropical Atlantic, and further south to approximately 15°S over the Indian Ocean and the Maritime Continents, which is closely related to the Walker Circulation. In this tropical zonal circulation air rises over the Maritime Continents (together with deep convection) and descends over the eastern Pacific (Bjerknes, 1969). Similar zonal circulation is found over the Atlantic with rising due to radiative heating over tropical Africa and South America and sinking due to radiative cooling over the tropical Atlantic (Julian and Chervin, 1978). The longitudinal variation of ozone at 430 hPa in the tropics is in agreement with the changes of $StratO_3/O_3$, showing ozone minimum over Maritime Continents as well as elevated ozone over eastern Pacific and Atlantic. Within the Atlantic, despite the smaller stratospheric contribution, the tropics have higher ozone mixing ratio (>80 ppb) than the subtropics at 430 hPa, and other sources must also contribute to the ozone maximum over tropical south Atlantic. Ozone over the tropical southeastern Pacific is also slightly elevated. The maximum stratospheric influence is found over the southern Indian and Pacific Oceans centered on 30°S, co-located with the tropospheric O_3 maximum over these regions. Both ozone and $StratO_3/O_3$ over the subtropics show strong longitudinal variations, with the co-located maxima over the south Indian Ocean. The ozone minimum at 430 hPa at 30°S occurs over the eastern Pacific region, while the minimum contribution of the stratospheric input is over the south Atlantic region. Given the spatial variations of the maximum/minimum in $StratO_3/O_3$ ratio and ozone mixing ratio, we separate the southern hemispheric ozone maximum into four sub-regions: 1) Tropical southeastern Pacific (0-20°S, 150°W-60°W); 2) Tropical South Atlantic (0-15°S, 60°W-40°E); 3) Subtropical South Atlantic (15°S-45°S, 60°W-40°E); 4) Subtropical South Indian Ocean (15°S-45°S, 40°E-150°E). We show in Figure 3 the maps of the IAV of simulated O_3 at 270 hPa and 430 hPa. The IAV is represented by the standard deviation of ozone anomalies (removing the monthly mean averaged from 1992 to 2011) over 1992-2011. Relatively stronger ozone IAV happens

over subtropical south Atlantic and subtropical south Indian Ocean at 270 hPa. At 430 hPa, tropical southeastern Pacific and tropical South Atlantic has slightly larger IAV. In this paper, we examine and quantify the relative roles of dynamics and chemistry on the IAV of tropospheric ozone variations over these selected regions during the past twenty years.

Figure 4 compares the anomalies of modeled and assimilated upper tropospheric ozone columns (UTOC, integrated from 500 hPa to the tropopause) as well as the anomalies of corresponding tropospheric ozone mixing ratio at 270 hPa and 430 hPa over two tropical sub-regions (tropical south Atlantic and tropical southeastern Pacific) from 2005 to 2011. The anomalies are calculated by removing the monthly mean averaged from 2005 to 2011. The short time scale variations in the model simulation tend to be greater compared to that in the assimilated ozone products, especially over the tropical south Atlantic region. But in general, the GMI-CTM hindcast simulation captures the assimilated IAV of the tropospheric ozone at these two levels as well as for the UTOC. Over the tropical south Atlantic, the modeled IAV agrees with the phase changes of assimilated ozone IAV but the simulation overestimates the assimilated ozone maximum in 2010 and underestimates the assimilated minima in 2007 and 2011 at both levels. Over the tropical southeastern Pacific, the IAV is influenced by ENSO related changes in dynamics (e.g., Ziemke et al., 2010;2011; Oman et al., 2013). The simulation reproduces much of the assimilated IAV, showing high ozone anomalies after 2005, 2010 La Nina year and negative ozone anomalies after strong El Niño year in 2009. However, during October 2006 to January 2007, the simulation shows a pronounced ozone peak, especially at 270 hPa, which is not seen in the assimilated ozone. Logan et al. (2008) examined interannual variations of tropospheric ozone profiles in October-December between 2005 and 2006 based on the satellite observations from Tropospheric Emission Spectrometer (TES). The TES data agree with what we found in the GMI-CTM model simulation, showing ozone enhancement over the tropical southeastern Pacific (150°W-60°W, 0-12°S) region in November 2006 relative to 2005 (~5-10 ppb at 250 hPa and 0-5 ppb at 400 hPa, Figure 3 of Logan et al., 2008). The agreement between TES and GMI-CTM indicates a possible low bias of GMAO assimilated ozone during late 2006, as a result of the low sensitivity

of OMI (Wargan et al., 2015).

Figure 5 shows the similar comparison as Figure 4, but over the two subtropical regions. Over the South Atlantic region, the assimilated ozone has similar but stronger IAV than that over the tropical southeastern Pacific region, showing the largest ozone year-by-year variation (~20ppb at 270 hPa) from October 2009 to October 2010, and the GMI-CTM simulation reproduces this variation quite well. Over the South Indian region, our model reproduces most of the variations in magnitude and phase, but shows anti-phase variations in late 2006/early 2007, which substantially affected the calculated correlation coefficients between model and assimilated ozone. The simulated upper tropospheric ozone column reproduces well the IAV in the assimilated ozone column except for the late 2006. In general, agreement between the simulated and assimilated results confirms the suitability of the model for investigations of the controlling factors on the tropospheric ozone IAV over these regions.

The left column of Figure 6 presents the monthly profiles of correlation coefficients between the simulated ozone and $StratO_3$ over the four sub-regions. Strong positive correlations between $StratO_3$ and O_3 are observed in most seasons in the upper troposphere even over two tropical regions. Stratospheric influence plays a big role during austral winter-spring and reaches its seasonal maximum in August, when the subtropical jet system is strongest and moves to its northern-most location. Over the two subtropical regions, the strong stratospheric influence persists throughout the whole troposphere ($r > 0.8$ at 700 hPa) in August. Over tropical south Atlantic region, the strong stratospheric influence is limited to the upper troposphere in austral winter-spring and decreases sharply with decreasing altitude. Over the tropical southeastern Pacific, the strong stratospheric influence persists year-long at the upper troposphere and reaches as low as ~400 hPa except for December.

The right column of Figure 6 shows the seasonal profiles of correlation coefficients between ozone and ozone from emissions ($EmissO_3$). The $EmissO_3$ is the difference between the simulations with varied and constant emission. Over the two subtropical regions, there are two seasonal maxima in the correlations between ozone and $EmissO_3$. The first occurs in September at the lower troposphere and decreases with increasing altitude, the second is in December/January showing opposite vertical gradient with

stronger correlations in the upper and middle troposphere. Over the tropical southeastern Pacific region, the influence from emissions shows a similar double-peak pattern, but with the first maximum localized at the surface and the second peak localized in the upper troposphere. Over the tropical south Atlantic, the influence of emissions is very small. South America and southern Africa are two major nearby burning regions. Emissions over South America have much larger IAV than those over southern Africa, although African emissions are larger in absolute terms (Sauvage et al., 2007; Liu et al., 2010; Voulgarakis et al., 2015). Sauvage et al (2007) argued that emissions over South and Southeast Asia could be transported southward in the upper troposphere through the Tropical Easterly Jet and affect ozone over Africa, the Atlantic and Indian Ocean (Hoskins and Rodwell, 1995; Rodwell and Hoskins, 2001). Meanwhile, emissions over this region also show large IAV (Voulgarakis et al., 2015). Therefore, the interannual emission changes in South America (0-20°S, 72.5°W-37.5°W), southern Africa (5°S-20°S, 12°E-38°E) and South and Southeast Asia (70°E-125°E, 10°S-40°N) may all affect the IAV of ozone due to emission changes in the southern hemisphere. In this study, we rely on tagged CO simulation to quantify the influence of biomass burning emissions from these three burning regions during months when emission IAV contributes significantly to the IAV of ozone.

In the next section, we choose August (the seasonal maximum of stratospheric input into the lower troposphere), September and December (the seasonal maximum of emission contribution) as three example months to examine the relative roles of different factors on IAV of tropospheric ozone over these regions.

3.3 Factors controlling IAV in ozone in the middle and upper troposphere

3.3.1 South Atlantic Region

Figure 7 shows the multiple regression results over the South Atlantic region. It compares the simulated ozone anomalies to that calculated from two regression variables: $StratO_3$ and $EmissO_3$ at 270 hPa and 430 hPa in August, September and December. The fitted ozone anomalies in generally reproduce the IAV obtained from the GMI-CTM simulation. The explained proportion of variability in simulated ozone anomalies by

372 $StratO_3$ and $EmissO_3$ is mostly above 50% and reaches as high as ~ 76% in December at
373 270 hPa, which demonstrates that $StratO_3$ and $EmissO_3$ are sufficient to explain the IAV
374 of tropospheric ozone over the south Atlantic region. In August at 430 hPa, the fitted
375 ozone anomalies have a slightly weaker correlation with the simulated ozone and show
376 less IAV compared to the ozone anomalies in GMI-CTM.
377 Figure 8 exhibits regression results in a way that highlights the relative contributions of
378 the IAV of stratospheric input and emission on the IAV of ozone over South Atlantic.
379 The three panels represent results from August, September and December from 1992 to
380 2011. Each panel has two columns, which illustrate the respective contribution from
381 changes in $StratO_3$ and $EmissO_3$ on the IAV of ozone mixing ratio. The left column of
382 each panel compares the anomalies of $StratO_3$ (blue) and simulated ozone mixing ratio
383 (black) from the GMI-CTM model at 270 and 430 hPa. The right column compares the
384 simulated O_3 residual after removing the regression from $StratO_3$ (black line) and
385 $EmissO_3$ (green line) at these two levels. The regression coefficient (β) and its 95%
386 confidence level are labeled in each panel and help us to determine whether the
387 corresponding contribution is significant to explain the variation of simulated ozone. As
388 discussed before, $EmissO_3$ reflects the effects from surface emission changes on ozone
389 variations at interannual time scale. The stratospheric input reaches its seasonal
390 maximum in August, during which the stratospheric contribution is significant
391 throughout the troposphere, explaining about 66% of the simulated ozone variance at 270
392 hPa and 37% at 430 hPa. The contributions from emission changes are very small and
393 insignificant at these two levels in August. In September, the IAV of stratospheric input
394 explains about 55% of the IAV in ozone at 270 hPa. The contribution decreases but is
395 still significant at 430 hPa. The IAV of surface emissions contributes substantially to the
396 IAV of ozone in September. The influence of emissions exceeds that of the stratosphere
397 and explains about 35% of IAV in ozone at 430hPa. In December, the contribution from
398 stratospheric input to the IAV of ozone is dominant (~47%) at 270 hPa. The contribution
399 from emission is also significant at this level and explains 28% variance of IAV of ozone.
400 At 430 hPa, the contribution from emission exceeds that from stratospheric input.
401 We quantify emission contributions from three burning regions using a tagged CO
402 simulation. Figure 9 shows standardized anomalies of the tagged CO tracers over South

Atlantic from three burning source regions, including southern Africa (red), South America (blue) and South and Southeast Asia (green) and their comparison with the $EmissO_3$ at 270 and 430 hPa in September and December from 1992 to 2011. The direct downwind transport of emissions from South America contributes most to the ozone variability from emissions over this region in September at both levels and the effects are most significant in the lower level (~58% at 430 hPa). In the upper troposphere, besides the contribution from S. America, the uplift and cross-equator transport of pollutants from South and Southeast Asia also contributes (>10%) to the ozone variation over South Atlantic region. The contribution from southern Africa is small and less than 10% at both levels. We also note that both $StratO_3$ and $EmissO_3$ show a minimum in 2009 and a maximum in 2010. There was a strong El Niño event in the year 2009/2010. Neu et al. (2014) identified the increased stratospheric circulation in 2010 driven by El Niño/easterly QBO based on TES data. A few other studies (e.g., Chen et al., 2011; Lewis et al., 2011) found that combined effects of 2009/2010 El Niño and warmer than normal Atlantic SST produced a severe drought over S. America and caused extensive biomass burning emission in 2010 dry season. Therefore, the agreements between changes in the $StratO_3$ and $EmissO_3$ over 2009/2010 are at least partly driven by ENSO. Similar tropospheric ozone anomalies are observed after 1997 and 2006 El Niño event. Olsen et al. (2016) examined the magnitude and spatial distribution of ENSO effects on tropospheric column ozone using the assimilated fields and found a statistically significant negative response of tropospheric column ozone to the Niño 3.4 index over South Atlantic Ocean.

In December, emissions from South America and southern Africa do not contribute substantially to the IAV of $EmissO_3$. Emissions from South and Southeast Asia dominate, explaining 83% and 77% variance of $EmissO_3$ IAV at 270 hPa and 430 hPa. The pollutants from South and Southeast Asia have the stronger influence at the upper troposphere because of their transport pathway as discussed in Sauvage et al. (2007). Therefore, the emission contribution of tropospheric ozone IAV becomes significant at 270 hPa in December.

In summary, over the South Atlantic region, the stratospheric input plays a dominant role in the upper troposphere with a seasonal maximum in August. At 430 hPa the

contribution from emission changes to the IAV of ozone exceeds that of stratospheric input in September and December. A tagged CO simulation from 1992 to 2011 shows the direct downwind transport of pollutants from South America is the largest contributor to $EmissO_3$ in September, and it is strongest near the surface. In December, cross-equator transport of South and Southeast Asia pollutants is the most important source of IAV due to emissions, and the effects are stronger in the upper troposphere.

3.3.2 South Indian Ocean

Over the south Indian Ocean, the fitted and simulated ozone anomalies are in excellent agreement (Figure 10). The explained proportion of variability in simulated ozone anomalies by $StratO_3$ and $EmissO_3$ is as high as ~ 88% in August at 270 hPa. We show relative contribution to the IAV in ozone due to stratospheric input and emission as obtained from multiple linear regression in Figure 11. In August and September, stratospheric input contributes more than 85% to ozone IAV at 270 hPa. The stratospheric contribution decreases slightly but is still dominant and significant at 430 hPa (~49% in August and 60% in September). The emission contribution, which is mainly from downwind transport of pollutants from S. America and southern Africa (Figure 12), is most important at 430 hPa in September but accounts for only 13% of ozone IAV. The emission contribution is smaller in August. In December, both stratospheric input and surface emission influence the IAV of ozone. The contribution from stratospheric input exceeds that from emissions at 270 hPa and becomes slightly weaker at 430 hPa. Examining the tagged sources simulation shows that emissions from South and Southeastern Asia regions are the largest source of ozone IAV at 270 hPa and 430 hPa in December with a stronger influence at the upper troposphere (Figure 12).

These results show that stratospheric ozone makes a significant contribution to the tropospheric ozone variability over the South Indian Ocean, with the largest influence in the upper troposphere in austral winter. Emission influence from nearby pollution in the boundary layer is relatively weak and only significant in September, one month after the southern hemisphere peak-burning season. In the upper troposphere, the cross-equator transport of pollutants from South and Southeast Asia is the major emission source

affecting the ozone variability. The influence peaks in December in the upper troposphere and extends to the middle troposphere.

3.3.3 Tropical South Atlantic

In the upper troposphere, lightning produces nitrogen oxides (NO_X) and promotes the photochemical ozone production (e.g., Pickering et al., 1993). Murray et al. (2013) shows that the IAV of tropical tropospheric ozone column is sensitive to the IAV of lightning over the tropical south Atlantic region. We therefore add the lightning NO_X as the third variable besides $StratO_3$ and $EmissO_3$. We test whether the addition of lightning NO_X improves the regression model significantly. Figure 13 shows the comparison between simulated and fitted ozone anomalies without and with lightning NO_X. During the "dry season" months of August and September, when the subtropical jet related STE (Karoly et al., 1998;Bals-Elsholz et al., 2001;Nakamura and Shimpo, 2004) reaches a seasonal maximum, the lightning activity reaches a seasonal minimum over the southern hemisphere. The fitted ozone anomalies based solely on $StratO_3$ and $EmissO_3$ (red) show high correlations ($r = 0.8$ in August, $r = 0.74$ in September) with that simulated from GMI-CTM at 270 hPa. Agreement between simulated and fitted ozone does not change in August and improves slightly in September by adding lightning NO_X in regression. In September, the simulated ozone anomaly shows a minimum (~ -6 ppb) in 2007 and a peak (~ 5ppb) in 2010 at 430 hPa, but the IAV from 2007 to 2010 is almost missing in the fitted ozone anomaly, which indicates that other factors drive the IAV of ozone over tropical south Atlantic during this period. During the "wet season" month of December, the lightning activity reaches its seasonal maximum. Our regression based on $StratO_3$ and $EmissO_3$ does not capture well the IAV of GMI-CTM simulated ozone at either level. The fitted ozone reproduces many of the IAV of simulated ozone after including lightning NO_X in the regression, indicating a strong influence from the lightning NO_X in December.

Figure 14 shows the regression results of relative contributions of stratospheric input and surface emission on the IAV of ozone. As discussed above, the tropical south Atlantic is in the descending branch of the Walker Circulation. Therefore, even though this region is located in the tropics, the IAV of stratospheric input still plays a dominant role and

493 explains 60% in August and 51% in September of ozone variance in the upper
494 troposphere. The stratospheric contribution, associated with radiative descent over this
495 region, drops to less than 38% in August and 18% in September at 430 hPa but is still
496 significant during these two months. Emission influence is significant at 430 hPa in
497 August but only account for 10% of ozone variation. Emission contribution is not
498 significant at either level in September. Examination of the simulation shows that
499 emission contribution is limited even at lower levels; the emission contribution becomes
500 significant and explains ~30% variance of ozone at ~700 hPa (not shown). In December,
501 neither stratospheric input nor emission contributes much to the IAV of ozone.
502 In the model, the lightning emissions take place in connection with deep convective
503 events (Allen et al., 2010). Increase in deep convection produces more upper tropospheric
504 NO_X from lightning, which results in more ozone production. On the other hand, deep
505 convection affects the upper tropospheric ozone budget through its direct transport of
506 surface air. In December, biomass burning in the Southern Hemisphere is at its seasonal
507 minimum. Air over tropical south Atlantic is relatively clean with low CO (Liu et al.,
508 2010). Deep convection over a clean region reduces upper tropospheric ozone by mixing
509 up ozone-poor air from near the surface. This effect could be opposite if deep convection
510 happens over a polluted region with relatively high ozone and its precursors (Lawrence et
511 al., 2003; Ziemke, et al., 2015). Use of the correlation to identify influence from the
512 lightning NO_X does not separate the two outcomes of IAV in convection, thus the sign of
513 the correlation between variations in lightning NO_X and upper tropospheric ozone can be
514 positive or negative. The correlation is positive if the contribution from lightning NO_X
515 exceeds the contribution from convective transport or if transport of polluted air increases
516 ozone. The correlation is negative if transport of clean air overwhelms ozone production
517 from lightning NO_X. Figure 15 compares the model residual after removing the
518 contributions from $StratO_3$ and $EmissO_3$ with the lightning NO_X at 270 hPa in September
519 and December. In September the IAV of lightning plays a minor but significant role in
520 the IAV of ozone in the upper troposphere. In December, the changes in lightning NO_X
521 have a significant impact on the ozone IAV, but show a negative regression (β_3=-1.29),
522 which indicates that the transport and mixing of clean surface air exceeds ozone

production from lightning NO_X emissions with a net negative impact of IAV in convection.

3.3.4 Tropical southeastern Pacific

Figure 16, 17 and 18 show the similar comparisons but over the tropical southeastern Pacific region. The fitted ozone anomalies show moderate but still significant correlations with that simulated from GMI-CTM in August and September. In December, the fitted ozone IAV agrees very well with the GMI-CTM simulated ozone IAV at 270 hPa. At 430 hPa the agreement collapses and the fitted ozone does not show strong IAV as seen in the GMI-CTM simulated ozone (Figure 16). Figure 17 shows that IAV in stratospheric input significantly affects the ozone IAV during these three months, explaining 28-40% of the variance of simulated ozone at 270 hPa. Emissions contribution is quite small in August and September, but is significant and explains 17% of simulated ozone IAV in December at 270 hPa. The tagged CO simulations show that the tropical southeastern Pacific region is influenced by nearby pollutants from South America, and also by the cross-equator transport of pollutants from South and Southeast Asia (Figure 18). Previous studies (e.g., Chandra et al., 1998; Sudo and Takahashi, 2001; Chandra et al., 2002; Ziemke and Chandra, 2003; Doherty et al., 2006; Chandra et al., 2009; Oman et al., 2011) show that ENSO has its strongest impact in the tropical Pacific basin. In August, the ITCZ is located at its northernmost location north of the Equator. Radiative sinking motion still dominates over the tropical southeastern Pacific in the middle - upper troposphere (Liu et al., 2010). Therefore, the emissions contribution from South America is quite small at 430 hPa and 270 hPa as shown in Figure 17. During an El Niño year, warmer SST with increased convection and large-scale upwelling begin in August, inhibiting the radiative sinking motion and resulting in ozone decrease in the middle-upper troposphere over this region. Our comparison shows strong negative correlation in August between IAV of middle-upper tropospheric ozone anomalies over this region and Niño 3.4 index during the past twenty years (Figure 19).

4 Summary and Discussion

Both model simulations and GEOS-5 assimilated ozone product derived from OMI/MLS show a tropospheric ozone column maximum centered over the south Atlantic from the equator to 30°S. This ozone maximum extends westward to South America and the eastern equatorial Pacific; it extends southeastward to southern Africa and the south Indian Ocean. In this study, we use hindcast simulations from the GMI-CTM, driven by assimilated MERRA meteorological fields, to interpret and quantify the relative importance of the stratospheric input and surface emission to the interannual variations of tropospheric ozone over four sub-regions of the SHTOM from 1992 to 2011. Over the SHTOM region, IAV in the stratospheric contribution is found to be the most important factor driving the IAV of ozone, especially over the upper troposphere, where O_3 changes have strong radiative effects (Lacis et al., 1990). The IAV of the stratospheric contribution explains a large portion of variance in the tropospheric ozone especially during the austral winter season, even over two selected tropical regions. The strong influence of emission on ozone IAV is largely confined to the South Atlantic region in September.

Although the SHTOM looks like a continuous feature in the southern hemisphere, our study shows that the relative importance between stratospheric input and surface emissions changes over different subregions at different altitude. Over the two extra-tropics regions, the IAV of stratospheric contribution explains at least 50% of variance of the tropospheric ozone during its winter season. The IAV of ozone over the south Indian Ocean is dominantly driven by the IAV of stratospheric ozone contribution with little or no influence from surface emissions at 270 hPa and 430 hPa. Over the south Atlantic region, besides the stratospheric ozone input, the IAV of surface emissions from South America and southern Africa also play a big role on the IAV of ozone, especially in the lower levels. The influence from emission exceeds that from the stratospheric contribution on the ozone variability in September at 430 hPa. In December, the emission influence mainly from remote transport of pollutants from South and Southeast Asia is significant and stays high in the upper troposphere.

Compared to the extra-tropics regions, the influence from stratospheric input is smaller but still significant in two tropical regions at both 270 hPa and 430 hPa in August and September. Over tropical south Atlantic region, the IAV of stratospheric input plays a

582 dominant role and explains 60% in August and 51% in September of the ozone IAV at
583 270 hPa. The stratospheric contribution is still significant at 430 hPa, but drops to less
584 than half of that at 270 hPa. Emission contributions are not significant at these two levels,
585 even during September. Our model shows that the IAV of ozone is partially driven by the
586 IAV of lightning in September. In December, the changes in lightning NO_X have a
587 significant impact on the ozone IAV, but show a negative correlation, which indicates
588 that the transport and mixing of clean surface air exceeds ozone production from
589 lightning NO_X emissions with a net negative impact of IAV in convection. Over the
590 tropical southeastern Pacific, IAV in stratospheric input significantly affects the ozone
591 IAV during these three months, explaining 28-40% of the variance of simulated ozone at
592 270 hPa. Emissions have little or no influence in August, September at 270 hPa and 430
593 hPa, but are significant in December at 270 hPa, explaining 17% of simulated ozone
594 IAV. A further comparison of ozone and ENSO index shows that ENSO, which affects
595 the tropical convection and large-scale upwelling, shows a strong negative correlation
596 with the IAV of tropospheric ozone over this region. Therefore, the model
597 simulations/predictions with different convective parameterizations exhibit large
598 uncertainties over this region as observed in Stevenson et al. (2006) and Young et al.
599 (2013).
600 In this study, our regional analysis based on the GMI-CTM model provides valuable
601 conclusions on drivers of interannual variability over different subregions of the SHTOM
602 and how they vary with the altitude. The quantification of their relative contributions on
603 interannual time scales enhances our understanding of the IAV and, potentially, long-
604 term trends in the tropospheric ozone and furthermore their effects on the radiative
605 forcing of climate.

606 **Acknowledgement**

607 All model output used for this article can be obtained by contacting J. Liu (email:
608 junhua.liu@nasa.gov). I gratefully acknowledge the financial support by NASA's
609 Atmospheric Chemistry Modeling and Analysis Program (ACMAP) (grants
610 NNH12ZDA001N). Work was performed under contract with NASA at Goddard. I

would like to thank K. Pickering, L. Oman, A. Thompson, H. Liu for their helpful discussion.

References

Allen, D., Pickering, K., Duncan, B., and Damon, M.: Impact of lightning NO emissions on North American photochemistry as determined using the Global Modeling Initiative (GMI) model, Journal of Geophysical Research-Atmospheres, 115, 10.1029/2010jd014062, 2010.

Bals-Elsholz, T. M., Atallah, E. H., Bosart, L. F., Wasula, T. A., Cempa, M. J., and Lupo, A. R.: The wintertime Southern Hemisphere split jet: Structure, variability, and evolution, Journal of Climate, 14, 4191-4215, 10.1175/1520-0442(2001)014<4191:twshsj>2.0.co;2, 2001.

Bjerknes, J.: Atmospheric teleconnections from the equatorial Pacific, Mon. Weather Rev., 97(3), 163–172, 1969.

Chandra, S., Ziemke, J. R., Min, W., and Read, W. G.: Effects of 1997-1998 El Nino on tropospheric ozone and water vapor, Geophysical Research Letters, 25, 3867-3870, 10.1029/98gl02695, 1998.

Chandra, S., Ziemke, J. R., Bhartia, P. K., and Martin, R. V.: Tropical tropospheric ozone: Implications for dynamics and biomass burning, Journal of Geophysical Research-Atmospheres, 107, 10.1029/2001jd000447, 2002.

Chandra, S., Ziemke, J. R., Duncan, B. N., Diehl, T. L., Livesey, N. J., and Froidevaux, L.: Effects of the 2006 El Nino on tropospheric ozone and carbon monoxide: implications for dynamics and biomass burning, Atmospheric Chemistry and Physics, 9, 4239-4249, 2009.

Chen, Y., Randerson, J. T., Morton, D. C., DeFries, R. S., Collatz, G. J., Kasibhatla, P. S., Giglio, L., Jin, Y., and Marlier, M. E.: Forecasting Fire Season Severity in South America Using Sea Surface Temperature Anomalies, Science, 334, 787-791, 10.1126/science.1209472, 2011.

Chevan, A., and Sutherland, M.: HIERARCHICAL PARTITIONING, American Statistician, 45, 90-96, 10.2307/2684366, 1991.

Chin, M., Ginoux, P., Kinne, S., Torres, O., Holben, B. N., Duncan, B. N., Martin, R. V., Logan, J. A., Higurashi, A., and Nakajima, T.: Tropospheric aerosol optical thickness from the GOCART model and comparisons with satellite and Sun photometer measurements, J ATMOS SCI, 59, 461-483, 2002.

Danielsen, E. F.: Stratospheric-Tropospheric Exchange Based on Radioactivity, Ozone and Potential VorticityStratospheric-Tropospheric Exchange Based on Radioactivity, Ozone and Potential Vorticity, Journal of the Atmospheric Sciences, 25, 502-518, 10.1175/1520-0469(1968).

Doherty, R. M., Stevenson, D. S., Johnson, C. E., Collins, W. J., and Sanderson, M. G.: Tropospheric ozone and El Nino-Southern Oscillation: Influence of atmospheric dynamics, biomass burning emissions, and future climate change, Journal of Geophysical Research-Atmospheres, 111, 10.1029/2005jd006849, 2006.

652 Duncan, B. N., Martin, R. V., Staudt, A. C., Yevich, R., and Logan, J. A.: Interannual and
653 seasonal variability of biomass burning emissions constrained by satellite
654 observations, Journal of Geophysical Research-Atmospheres, 108,
655 10.1029/2002jd002378, 2003.
656 Duncan, B. N., Strahan, S. E., Yoshida, Y., Steenrod, S. D., and Livesey, N.: Model study
657 of the cross-tropopause transport of biomass burning pollution, ATMOS CHEM
658 PHYS, 7, 3713-3736, 2007.
659 Eyring, V., Lamarque, J.-F., Hess, P., Arfeuille, F., Bowman, K., Chipperfield, M. P.,
660 Duncan, B., Fiore, A., Gettelman, A., Giorgetta, M. A., Granier, C., Kinnison, M.
661 H. D., Kunze, M., Langematz, U., Luo, B., Martin, R., Matthes, K., Newman, P.
662 A., Peter, T., Robock, A., Ryerson, T., Saiz-Lopez, A., Salawitch, R., Schultz, M.,
663 Shepherd, T. G., Shindell, D., Staehelin, J., Tegtmeier, S., Thomason, L., Tilmes,
664 S., Vernier, J.-P., Waugh, D. W., and Young, P. J.: Overview of IGAC/SPARC
665 Chemistry-Climate Model Initiative (CCMI) Community Simulations in
666 Support of Upcoming Ozone and Climate Assessments. In: SPARC
667 Newsletter 40, 48, WMO/SPARC, Zürich, 2013.
668 Fishman, J., Watson, C. E., Larsen, J. C., and Logan, J. A.: DISTRIBUTION OF
669 TROPOSPHERIC OZONE DETERMINED FROM SATELLITE DATA, Journal
670 of Geophysical Research-Atmospheres, 95, 3599-3617,
671 10.1029/JD095iD04p03599, 1990.
672 Folkins, I., Braun, C., Thompson, A. M., and Witte, J.: Tropical ozone as an indicator of
673 deep convection, Journal of Geophysical Research-Atmospheres, 107,
674 10.1029/2001jd001178, 2002.
675 Groemping, U.: Two simple estimators of relative importance in linear regression based
676 on variance decomposition - Response, American Statistician, 61, 282-283, 2007.
677 Guenther, A., Karl, T., Harley, P., Wiedinmyer, C., Palmer, P. I., and Geron, C.:
678 Estimates of global terrestrial isoprene emissions using MEGAN (Model of
679 Emissions of Gases and Aerosols from Nature), ATMOS CHEM PHYS, 6, 3181-
680 3210, 2006.
681 Hess, P., and Mahowald, N.: Interannual variability in hindcasts of atmospheric
682 chemistry: the role of meteorology, ATMOS CHEM PHYS, 9, 5261-5280,
683 10.5194/acp-9-5261-2009, 2009.
684 Hoskins, B. J., and Rodwell, M. J.: A MODEL OF THE ASIAN SUMMER MONSOON
685 .1. THE GLOBAL-SCALE, Journal of the Atmospheric Sciences, 52, 1329-1340,
686 10.1175/1520-0469(1995)052<1329:amotas>2.0.co;2, 1995.
687 Jacob, D. J., Heikes, B. G., Fan, S. M., Logan, J. A., Mauzerall, D. L., Bradshaw, J. D.,
688 Singh, H. B., Gregory, G. L., Talbot, R. W., Blake, D. R., and Sachse, G. W.:
689 Origin of ozone and NOx in the tropical troposphere: A photochemical analysis of
690 aircraft observations over the South Atlantic basin, Journal of Geophysical
691 Research-Atmospheres, 101, 24235-24250, 10.1029/96jd00336, 1996.
692 Jenkins, G. S., and Ryu, J. H.: Space-borne observations link the tropical atlantic ozone
693 maximum and paradox to lightning, Atmospheric Chemistry and Physics, 4, 361-
694 375, 2004a.
695 Jenkins, G. S., and Ryu, J. H.: Linking horizontal and vertical transports of biomass fire
696 emissions to the tropical Atlantic ozone paradox during the Northern Hemisphere

winter season: climatology, Atmospheric Chemistry and Physics, 4, 449-469, 2004b.
Jourdain, L., Worden, H. M., Worden, J. R., Bowman, K., Li, Q., Eldering, A., Kulawik, S. S., Osterman, G., Boersma, K. F., Fisher, B., Rinsland, C. P., Beer, R., and Gunson, M.: Tropospheric vertical distribution of tropical Atlantic ozone observed by TES during the northern African biomass burning season, Geophysical Research Letters, 34, 10.1029/2006gl028284, 2007.
Julian, P. R., and Chervin, R. M.: A study of the Southern Oscillation and Walker Circulation phenomenon, Mon. Weather Rev., 106(10), 1433–1451, 1978.
Karoly, D. J., Vincent, D. G., and Schrage, J. M.: Meteorology of the Southern Hemisphere, General circulation, American Meteorological Society, 45 Beacon St., Boston, MA, 02108, 1998.
Kim, P. S., Jacob, D. J., Liu, X., Warner, J. X., Yang, K., Chance, K., Thouret, V., and Nedelec, P.: Global ozone-CO correlations from OMI and AIRS: constraints on tropospheric ozone sources, Atmospheric Chemistry and Physics, 13, 9321-9335, 10.5194/acp-13-9321-2013, 2013.
Kruskal, W.: RELATIVE IMPORTANCE BY AVERAGING OVER ORDERINGS, American Statistician, 41, 6-10, 10.2307/2684310, 1987.
Lacis, A. A., Wuebbles, D. J., and Logan, J. A.: RADIATIVE FORCING OF CLIMATE BY CHANGES IN THE VERTICAL-DISTRIBUTION OF OZONE, Journal of Geophysical Research-Atmospheres, 95, 9971-9981, 10.1029/JD095iD07p09971, 1990.
Lawrence, M. G., von Kuhlmann, R., Salzmann, M., and Rasch, P. J.: The balance of effects of deep convective mixing on tropospheric ozone, Geophysical Research Letters, 30, 10.1029/2003gl017644, 2003.
Lewis, S. L., Brando, P. M., Phillips, O. L., van der Heijden, G. M. F., and Nepstad, D.: The 2010 Amazon Drought, Science, 331, 554-554, 10.1126/science.1200807, 2011.
Lin, M., Fiore, A. M., Cooper, O. R., Horowitz, L. W., Langford, A. O., Levy II, H., Johnson, B. J., Vaishali Naik, V., Oltmans, S. J., and Senff, C. J.: Springtime high surface ozone events over the western United States: Quantifying the role of stratospheric intrusions, Submitted to JGR-Atmosphere, CalNex Special Section, 2012.
Liu, J., Logan, J. A., Jones, D. B. A., Livesey, N. J., Megretskaia, I., Carouge, C., and Nedelec, P.: Analysis of CO in the tropical troposphere using Aura satellite data and the GEOS-Chem model: insights into transport characteristics of the GEOS meteorological products, Atmospheric Chemistry and Physics, 10, 12207-12232, 10.5194/acp-10-12207-2010, 2010.
Liu, J., Logan, J. A., Murray, L. T., Pumphrey, H. C., Schwartz, M. J., and Megretskaia, I. A.: Transport analysis and source attribution of seasonal and interannual variability of CO in the tropical upper troposphere and lower stratosphere, Atmospheric Chemistry and Physics, 13, 129-146, 10.5194/acp-13-129-2013, 2013.
Liu, J., Rodriguez, J. M., Thompson, A. M., Logan, J. A., Douglass, A. R., Olsen, M. A., Steenrod, S. D., and Posny, F.: Origins of tropospheric ozone interannual

742 variation over Reunion: A model investigation, Journal of Geophysical Research-
743 Atmospheres, 121, 521-537, 10.1002/2015jd023981, 2016.
744 Logan, J. A., Prather, M. J., Wofsy, S. C., and McElroy, M. B.: TROPOSPHERIC
745 CHEMISTRY - A GLOBAL PERSPECTIVE, Journal of Geophysical Research-
746 Oceans and Atmospheres, 86, 7210-7254, 10.1029/JC086iC08p07210, 1981.
747 Logan, J. A., Megretskaia, I., Nassar, R., Murray, L. T., Zhang, L., Bowman, K. W.,
748 Worden, H. M., and Luo, M.: Effects of the 2006 El Nino on tropospheric
749 composition as revealed by data from the Tropospheric Emission Spectrometer
750 (TES), Geophysical Research Letters, 35, 10.1029/2007gl031698, 2008.
751 Martin, R. V., Jacob, D. J., Logan, J. A., Bey, I., Yantosca, R. M., Staudt, A. C., Li, Q.
752 B., Fiore, A. M., Duncan, B. N., Liu, H. Y., Ginoux, P., and Thouret, V.:
753 Interpretation of TOMS observations of tropical tropospheric ozone with a global
754 model and in situ observations, Journal of Geophysical Research-Atmospheres,
755 107, 10.1029/2001jd001480, 2002.
756 Murray, L. T., Logan, J. A., and Jacob, D. J.: Interannual variability in tropical
757 tropospheric ozone and OH: The role of lightning, Journal of Geophysical
758 Research-Atmospheres, 118, 11468-11480, 10.1002/jgrd.50857, 2013.
759 Nakamura, H., and Shimpo, A.: Seasonal Variations in the Southern Hemisphere Storm
760 Tracks and Jet Streams as Revealed in a Reanalysis Dataset., *J. Climate*, **17**,
761 1828–1844., 2004.
762 Neu, J. L., Flury, T., Manney, G. L., Santee, M. L., Livesey, N. J., and Worden, J.:
763 Tropospheric ozone variations governed by changes in stratospheric circulation,
764 Nature Geoscience, 7, 340-344, 10.1038/ngeo2138, 2014.
765 Olivier, J. G. J., Van Aardenne, J. A., Dentener, F. J., Pagliari, V., Ganzeveld, L. N., and
766 Peters, J. A. H. W.: Recent trends in global greenhouse gas emissions: regional
767 trends and spatial distribution of key sources, in: Non-CO2 Greenhouse Gases
768 (NCGG-4), coordinator: van Amstel, A., Millpress, Rotterdam, ISBN 905966
769 043 9, 325–330,, 2005.
770 Olsen, M. A., Wargan, K., and Pawson, S.: Tropospheric column ozone response to
771 ENSO in GEOS-5 assimilation of OMI and MLS ozone data, Atmospheric
772 Chemistry and Physics, 16, 7091-7103, 10.5194/acp-16-7091-2016, 2016.
773 Oman, L. D., Ziemke, J. R., Douglass, A. R., Waugh, D. W., Lang, C., Rodriguez, J. M.,
774 and Nielsen, J. E.: The response of tropical tropospheric ozone to ENSO,
775 Geophysical Research Letters, 38, 10.1029/2011gl047865, 2011.
776 Oman, L. D., Douglass, A. R., Ziemke, J. R., Rodriguez, J. M., Waugh, D. W., and
777 Nielsen, J. E.: The ozone response to ENSO in Aura satellite measurements and a
778 chemistry-climate simulation, Journal of Geophysical Research-Atmospheres,
779 118, 965-976, 10.1029/2012jd018546, 2013.
780 Pickering, K. E., Thompson, A. M., Tao, W. K., and Kucsera, T. L.: UPPER
781 TROPOSPHERIC OZONE PRODUCTION FOLLOWING MESOSCALE
782 CONVECTION DURING STEP EMEX, Journal of Geophysical Research-
783 Atmospheres, 98, 8737-8749, 10.1029/93jd00875, 1993.
784 Pickering, K. E., Thompson, A. M., Wang, Y. S., Tao, W. K., McNamara, D. P.,
785 Kirchhoff, V., Heikes, B. G., Sachse, G. W., Bradshaw, J. D., Gregory, G. L., and
786 Blake, D. R.: Convective transport of biomass burning emissions over Brazil

787 during TRACE A, Journal of Geophysical Research-Atmospheres, 101, 23993-
788 24012, 10.1029/96jd00346, 1996.
789 Prather, M. J., Zhu, X., Tang, Q., Hsu, J. N., and Neu, J. L.: An atmospheric chemist in
790 search of the tropopause, J GEOPHYS RES-ATMOS, 116, D04306,
791 10.1029/2010jd014939, 2011.
792 Rienecker, M. M., Suarez, M. J., Gelaro, R., Todling, R., Bacmeister, J., Liu, E.,
793 Bosilovich, M. G., Schubert, S. D., Takacs, L., Kim, G.-K., Bloom, S., Chen, J.,
794 Collins, D., Conaty, A., Da Silva, A., Gu, W., Joiner, J., Koster, R. D., Lucchesi,
795 R., Molod, A., Owens, T., Pawson, S., Pegion, P., Redder, C. R., Reichle, R.,
796 Robertson, F. R., Ruddick, A. G., Sienkiewicz, M., and Woollen, J.: MERRA:
797 NASA's Modern-Era Retrospective Analysis for Research and Applications,
798 Journal of Climate, 24, 3624-3648, 10.1175/jcli-d-11-00015.1, 2011.
799 Rodwell, M. J., and Hoskins, B. J.: Subtropical anticyclones and summer monsoons,
800 Journal of Climate, 14, 3192-3211, 10.1175/1520-
801 0442(2001)014<3192:saasm>2.0.co;2, 2001.
802 Sauvage, B., Thouret, V., Thompson, A. M., Witte, J. C., Cammas, J. P., Nedelec, P., and
803 Athier, G.: Enhanced view of the "tropical Atlantic ozone paradox" and "zonal
804 wave one" from the in situ MOZAIC and SHADOZ data, Journal of Geophysical
805 Research-Atmospheres, 111, 10.1029/2005jd006241, 2006.
806 Sauvage, B., Martin, R. V., van Donkelaar, A., and Ziemke, J. R.: Quantification of the
807 factors controlling tropical tropospheric ozone and the South Atlantic maximum,
808 Journal of Geophysical Research-Atmospheres, 112, 10.1029/2006jd008008,
809 2007.
810 Solomon, S., Thompson, D. W. J., Portmann, R. W., Oltmans, S. J., and Thompson, A.
811 M.: On the distribution and variability of ozone in the tropical upper troposphere:
812 Implications for tropical deep convection and chemical-dynamical coupling,
813 Geophysical Research Letters, 32, 10.1029/2005gl024323, 2005.
814 Stevenson, D. S., Dentener, F. J., Schultz, M. G., Ellingsen, K., van Noije, T. P. C., Wild,
815 O., Zeng, G., Amann, M., Atherton, C. S., Bell, N., Bergmann, D. J., Bey, I.,
816 Butler, T., Cofala, J., Collins, W. J., Derwent, R. G., Doherty, R. M., Drevet, J.,
817 Eskes, H. J., Fiore, A. M., Gauss, M., Hauglustaine, D. A., Horowitz, L. W.,
818 Isaksen, I. S. A., Krol, M. C., Lamarque, J. F., Lawrence, M. G., Montanaro, V.,
819 Muller, J. F., Pitari, G., Prather, M. J., Pyle, J. A., Rast, S., Rodriguez, J. M.,
820 Sanderson, M. G., Savage, N. H., Shindell, D. T., Strahan, S. E., Sudo, K., and
821 Szopa, S.: Multimodel ensemble simulations of present-day and near-future
822 tropospheric ozone, Journal of Geophysical Research-Atmospheres, 111,
823 10.1029/2005jd006338, 2006.
824 Stohl, A., Bonasoni, P., Cristofanelli, P., Collins, W., Feichter, J., Frank, A., Forster, C.,
825 Gerasopoulos, E., Gaggeler, H., James, P., Kentarchos, T., Kromp-Kolb, H.,
826 Kruger, B., Land, C., Meloen, J., Papayannis, A., Priller, A., Seibert, P., Sprenger,
827 M., Roelofs, G. J., Scheel, H. E., Schnabel, C., Siegmund, P., Tobler, L., Trickl,
828 T., Wernli, H., Wirth, V., Zanis, P., and Zerefos, C.: Stratosphere-troposphere
829 exchange: A review, and what we have learned from STACCATO, Journal of
830 Geophysical Research-Atmospheres, 108, 10.1029/2002jd002490, 2003.

Strahan, S. E., Duncan, B. N., and Hoor, P.: Observationally derived transport diagnostics for the lowermost stratosphere and their application to the GMI chemistry and transport model, ATMOS CHEM PHYS, 7, 2435-2445, 2007.

Strahan, S. E., Douglass, A. R., and Newman, P. A.: The contributions of chemistry and transport to low arctic ozone in March 2011 derived from Aura MLS observations, Journal of Geophysical Research-Atmospheres, 118, 1563-1576, 10.1002/jgrd.50181, 2013.

Strode, S. A., Rodriguez, J. M., Logan, J. A., Cooper, O. R., Witte, J. C., Lamsal, L. N., Damon, M., Van Aartsen, B., Steenrod, S. D., and Strahan, S. E.: Trends and variability in surface ozone over the United States, Journal of Geophysical Research-Atmospheres, 120, 9020-9042, 10.1002/2014jd022784, 2015.

Sudo, K., and Takahashi, M.: Simulation of tropospheric ozone changes during 1997-1998 El Nino: Meteorological impact on tropospheric photochemistry, Geophysical Research Letters, 28, 4091-4094, 10.1029/2001gl013335, 2001.

Thompson, A. M., Pickering, K. E., McNamara, D. P., Schoeberl, M. R., Hudson, R. D., Kim, J. H., Browell, E. V., Kirchhoff, V., and Nganga, D.: Where did tropospheric ozone over southern Africa and the tropical Atlantic come from in October 1992? Insights from TOMS, GTE TRACE A, and SAFARI 1992, Journal of Geophysical Research-Atmospheres, 101, 24251-24278, 10.1029/96jd01463, 1996.

Thompson, A. M., Witte, J. C., McPeters, R. D., Oltmans, S. J., Schmidlin, F. J., Logan, J. A., Fujiwara, M., Kirchhoff, V., Posny, F., Coetzee, G. J. R., Hoegger, B., Kawakami, S., Ogawa, T., Johnson, B. J., Vomel, H., and Labow, G.: Southern Hemisphere Additional Ozonesondes (SHADOZ) 1998-2000 tropical ozone climatology - 1. Comparison with Total Ozone Mapping Spectrometer (TOMS) and ground-based measurements, Journal of Geophysical Research-Atmospheres, 108, 10.1029/2001jd000967, 2003.

Thouret, V., Saunois, M., Minga, A., Mariscal, A., Sauvage, B., Solete, A., Agbangla, D., Nedelec, P., Mari, C., Reeves, C. E., and Schlager, H.: An overview of two years of ozone radio soundings over Cotonou as part of AMMA, Atmospheric Chemistry and Physics, 9, 6157-6174, 2009.

Tocquer, F., Barret, B., Mari, C., Le Flochmoen, E., Cammas, J. P., and Sauvage, B.: An upper tropospheric 'ozone river' from Africa to India during the 2008 Asian post-monsoon season, Tellus Series B-Chemical and Physical Meteorology, 67, 10.3402/tellusb.v67.25350, 2015.

van der Werf, G. R., Randerson, J. T., Giglio, L., Collatz, G. L., Mu, M., Kasibhatla, P. S., Morton, D. C., DeFries, R. S., Jin, Y., and T.T., v. L.: Global fire emissions and the contribution of deforestation, savanna, forest, agricultural, and peat fires (1997–2009), ATMOS CHEM PHYS, 10, 16153-16230, 2010.

Voulgarakis, A., Savage, N. H., Wild, O., Braesicke, P., Young, P. J., Carver, G. D., and Pyle, J. A.: Interannual variability of tropospheric composition: the influence of changes in emissions, meteorology and clouds, Atmospheric Chemistry and Physics, 10, 2491-2506, 10.5194/acp-10-2491-2010, 2010.

Voulgarakis, A., Hadjinicolaou, P., and Pyle, J. A.: Increases in global tropospheric ozone following an El Nino event: examining stratospheric ozone variability as a

potential driver, Atmospheric Science Letters, 12, 228-232, 10.1002/asl.318, 2011.
Voulgarakis, A., Marlier, M. E., Faluvegi, G., Shindell, D. T., Tsigaridis, K., and Mangeon, S.: Interannual variability of tropospheric trace gases and aerosols: The role of biomass burning emissions, Journal of Geophysical Research-Atmospheres, 120, 7157-7173, 10.1002/2014jd022926, 2015.
Wargan, K., Pawson, S., Olsen, M. A., Witte, J. C., Douglass, A. R., Ziemke, J. R., Strahan, S. E., and Nielsen, J. E.: The global structure of upper troposphere-lower stratosphere ozone in GEOS-5: A multiyear assimilation of EOS Aura data, Journal of Geophysical Research-Atmospheres, 120, 2013-2036, 10.1002/2014jd022493, 2015.
Weller, R., Lilischkis, R., Schrems, O., Neuber, R., and Wessel, S.: Vertical ozone distribution in the marine atmosphere over the central Atlantic Ocean (56 degrees S 50 degrees N), Journal of Geophysical Research-Atmospheres, 101, 1387-1399, 10.1029/95jd02838, 1996.
WMO: Scientific Assessment of Ozone Depletion: 2014, Global Ozone Research and Monitoring Project, World Meteorological Organization, Geneva, Switzerland, 2014.
Zeng, G., and Pyle, J. A.: Influence of El Nino Southern Oscillation on stratosphere/troposphere exchange and the global tropospheric ozone budget, Geophysical Research Letters, 32, 10.1029/2004gl021353, 2005.
Ziemke, J. R., Chandra, S., Thompson, A. M., and McNamara, D. P.: Zonal asymmetries in southern hemisphere column ozone: Implications of biomass burning, Journal of Geophysical Research-Atmospheres, 101, 14421-14427, 10.1029/96jd01057, 1996.
Ziemke, J. R., and Chandra, S.: La Nina and El Nino-induced variabilities of ozone in the tropical lower atmosphere during 1970-2001, Geophysical Research Letters, 30, 10.1029/2002gl016387, 2003.
Ziemke, J. R., Chandra, S., Oman, L. D., and Bhartia, P. K.: A new ENSO index derived from satellite measurements of column ozone, Atmospheric Chemistry and Physics, 10, 3711-3721, 2010.
Ziemke, J. R., Olsen, M. A., Witte, J. C., Douglass, A. R., Strahan, S. E., Wargan, K., Liu, X., Schoeberl, M. R., Yang, K., Kaplan, T. B., Pawson, S., Duncan, B. N., Newman, P. A., Bhartia, P. K., and Heney, M. K.: Assessment and applications of NASA ozone data products derived from Aura OMI/MLS satellite measurements in context of the GMI chemical transport model, Journal of Geophysical Research-Atmospheres, 119, 5671-5699, 10.1002/2013jd020914, 2014.
Ziemke, J.R., A.R. Douglass, L.D. Oman, S.E. Strahan, and B.N. Duncan, "Tropospheric ozone variability in the tropics from ENSO to MJO and shorter timescales", Atmos. Chem. Phys. Discuss., 15, 6373-6401, doi:10.5194/acpd-15-6373-2015, 2015.

Figures:

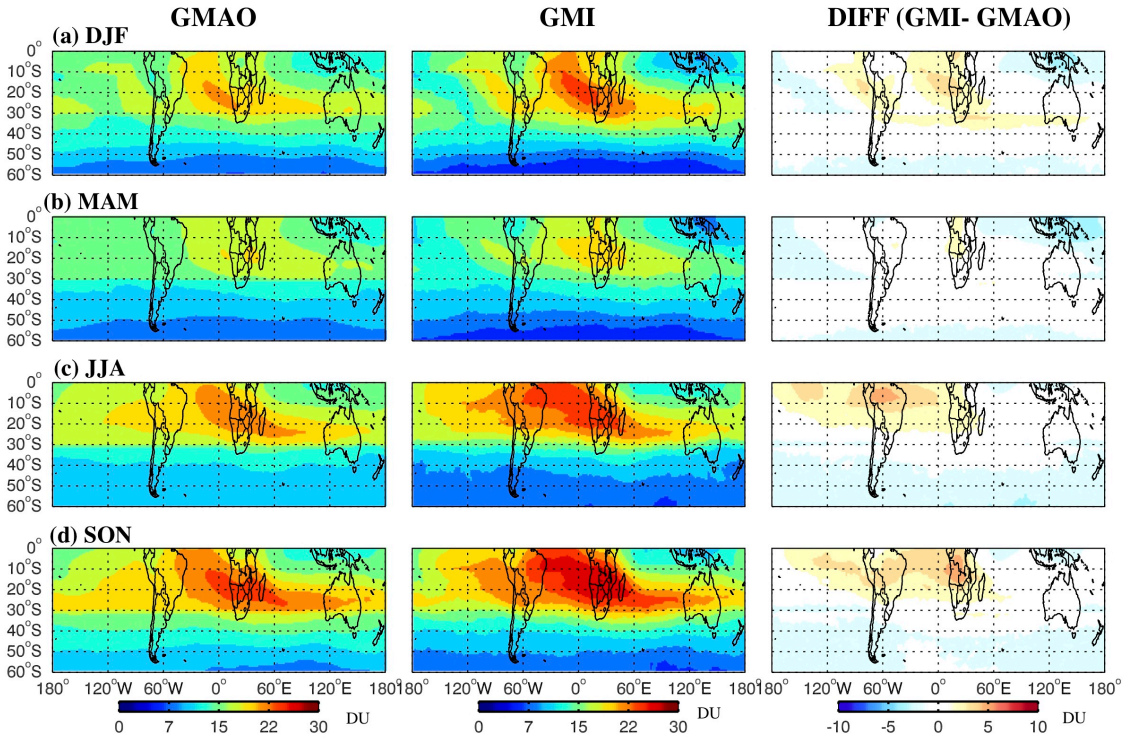

Figure 1: Seasonal climatology of upper tropospheric column ozone (UTOC, integrated from 500 hPa to the tropopause) (in Dobson Units) for (a) December-January-February (DJF), (b) March-April-May (MAM), (c) June-July-August (JJA), and (d) September-October-November (SON) averaged from 2005 to 2012 for GMAO assimilated ozone (left) and GMI-CTM Hindcast-VE ozone (middle) and their absolute difference (right). The GMAO assimilated ozone has been adjusted by adding 2.5 DU in 0-30° S based on Wargan et al. (2015).

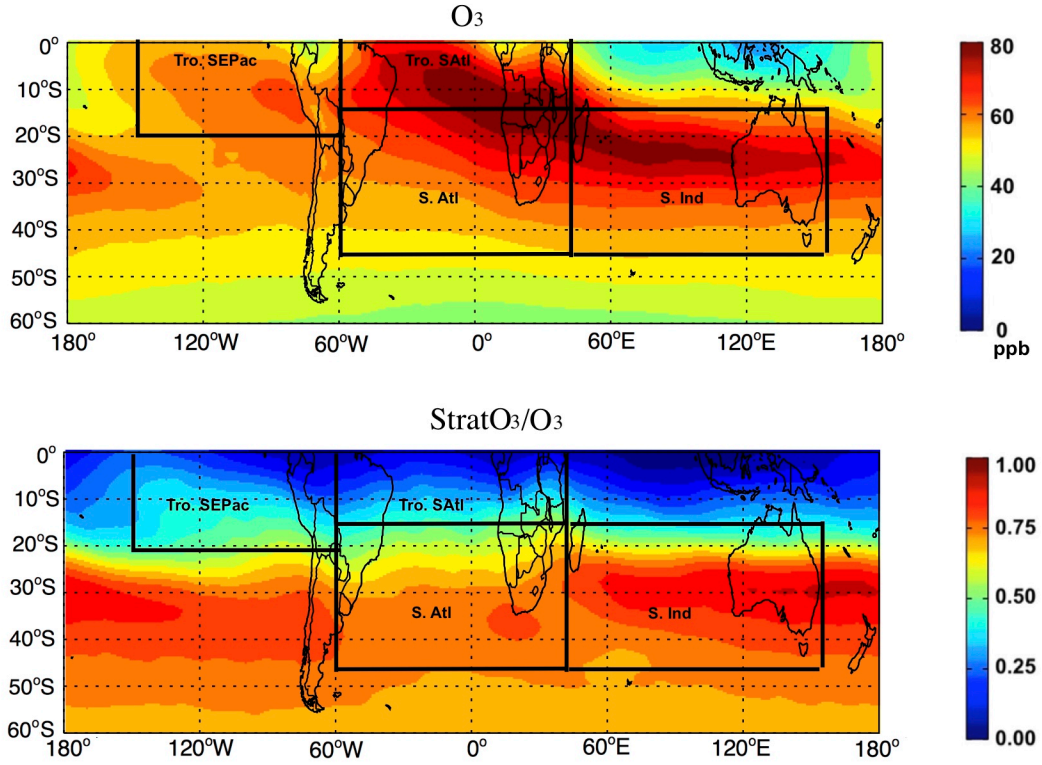

930

931 **Figure 2:** The simulated ozone (top) and the $StratO_3/O_3$ (bottom) at 430 hPa averaged
932 over 1992-2011 in September. Stronger stratospheric influence happens over southern
933 hemisphere centered on 30° S, co-locating with subtropical jet stream regions with
934 descending stratospheric air. The black boxes show four regions discussed in this study.
935 From left to right: (1) Tropical southeastern Pacific (0-20° S, 150° W-60° W); (2)
936 Tropical South Atlantic region (0-15° S, 60° W-40° E); (3) Subtropical South Atlantic
937 region (15° S-45° S, 60° W-40° E); (4) Subtropical South Indian Ocean (15° S-45° S, 40°
938 E-150° E).

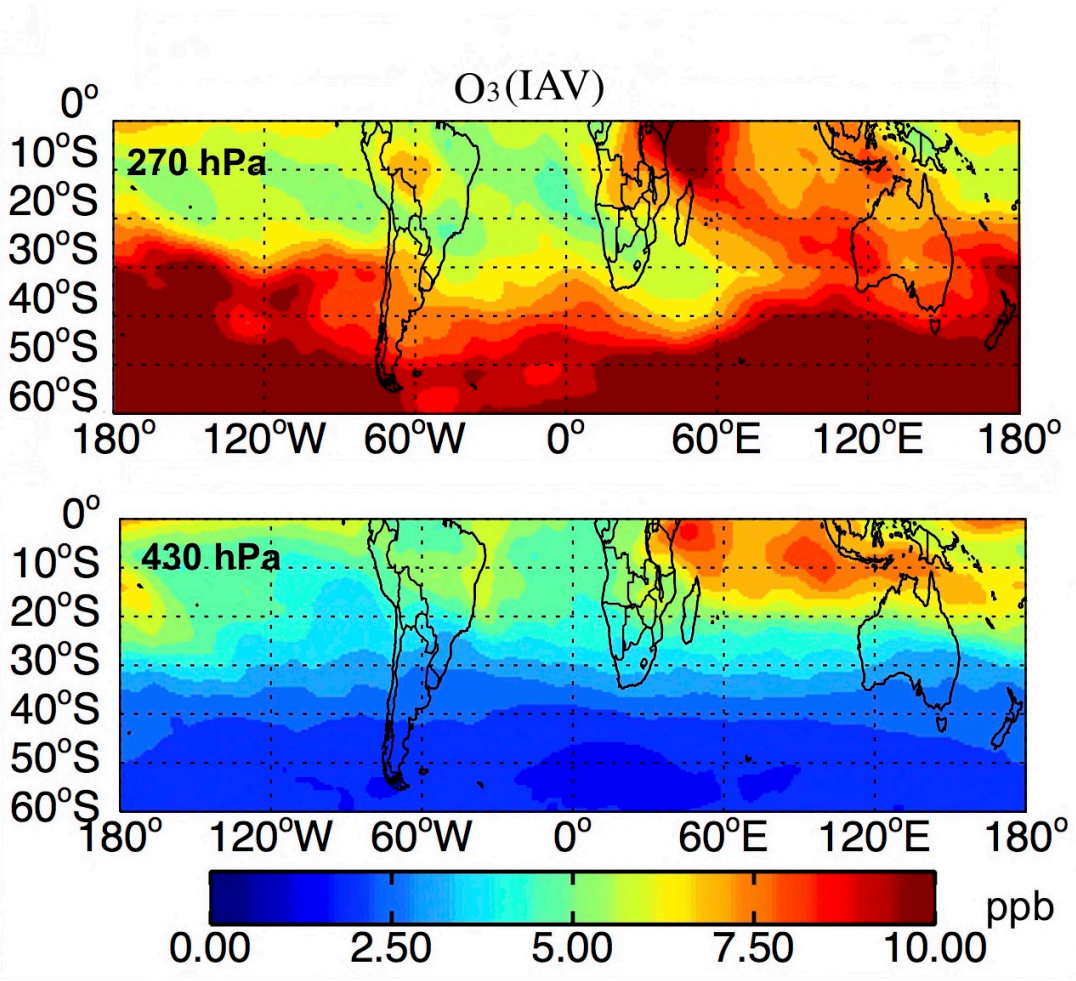

939

940 **Figure 3:** The interannual variations (IAV, unit of ppb) of simulated ozone at 270 hPa
941 (top) and 430 hPa (bottom). The standard deviation of ozone anomalies (removing the
942 monthly mean) over 1991-2011 represents the IAV.

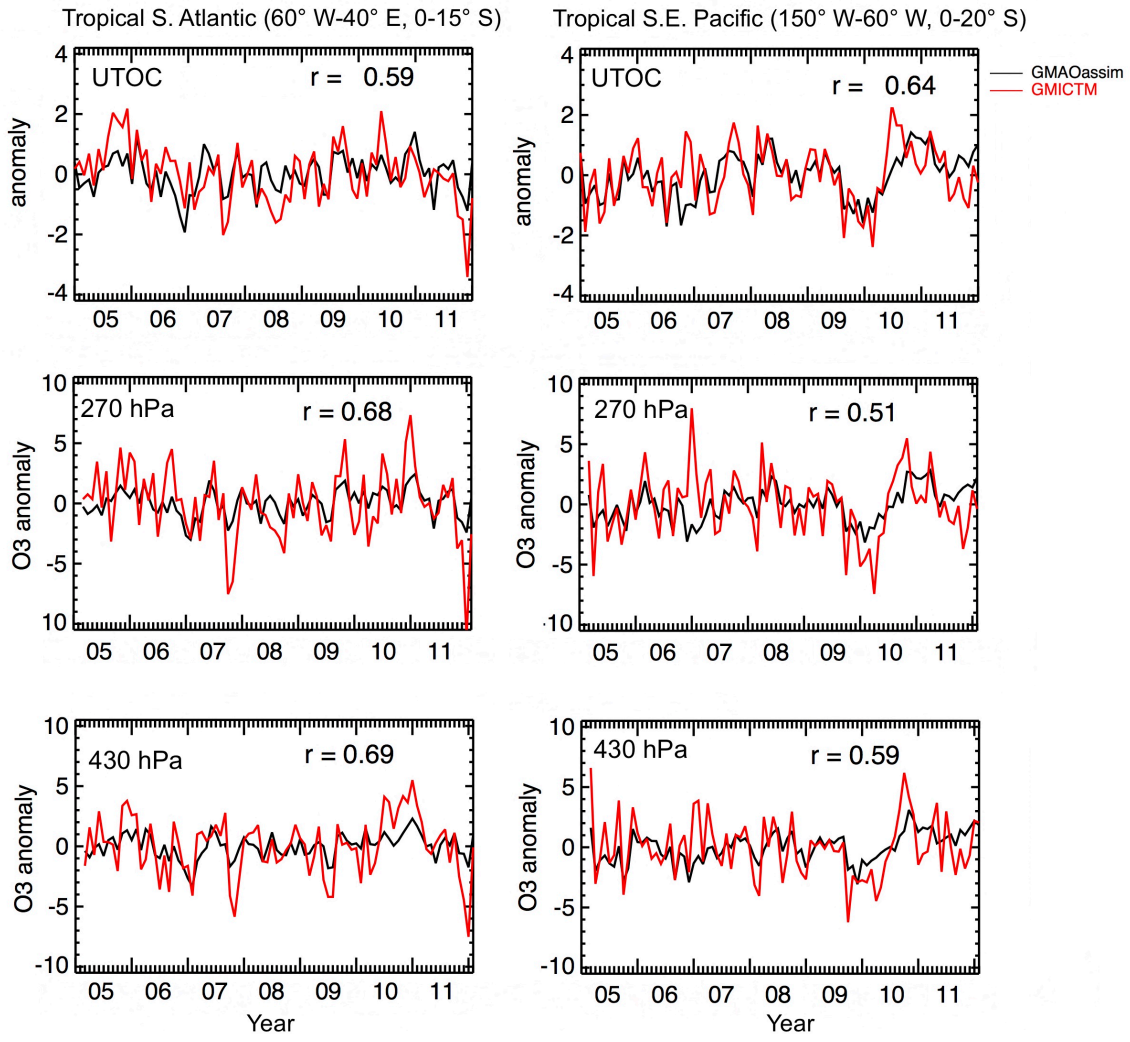

943

944 **Figure 4:** Time series plots of upper tropospheric ozone column (UTOC, integrated from
945 500 hPa to the tropopause; unit: DU) anomalies and tropospheric ozone anomalies (unit:
946 ppb) at 270 hPa and 430 hPa from GMAO assimilated data (black) and GMI-CTM (red)
947 over (left) Tropical South Atlantic region (60° W-40° E, 0-15° S); (right) Tropical
948 southeastern Pacific (150° W-60° W, 0-20° S) from 2005 to 2011. The anomalies are
949 calculated by removing the monthly mean averaged from 2005 to 2011.

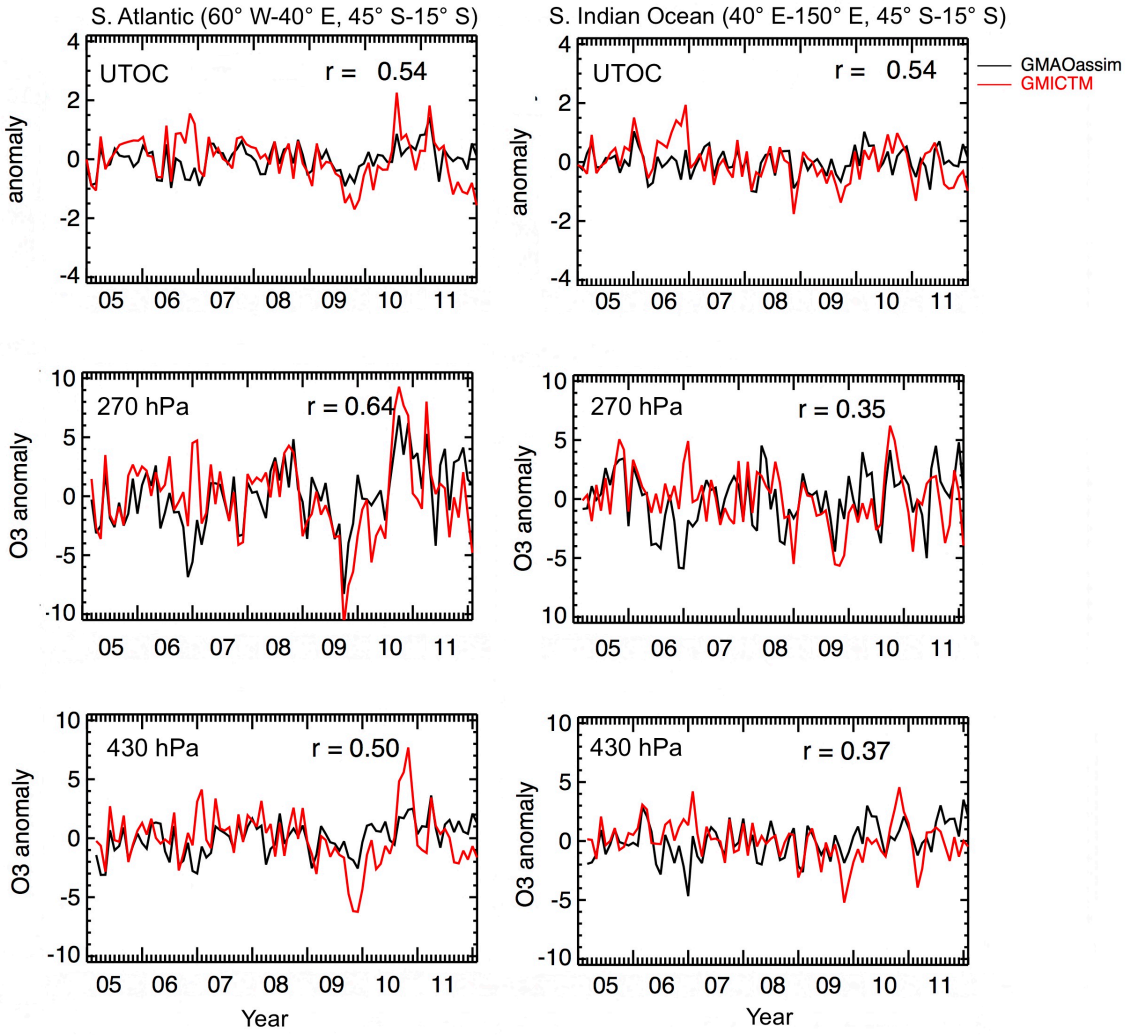

950
951 **Figure 5:** Time series plots of upper tropospheric ozone column (UTOC, integrated from
952 500 hPa to the tropopause; unit: DU) anomalies and tropospheric ozone anomalies (unit:
953 ppb) at 270 hPa and 430 hPa from GMAO assimilated data (black) and GMI-CTM (red)
954 over (left) South Atlantic (60° W-40° E, 15° S-45° S); (right) South Indian Ocean (40° E-
955 150° E, 15° S-45° S) from 2005 to 2011. The anomalies are calculated by removing the
956 monthly mean averaged from 2005 to 2011.

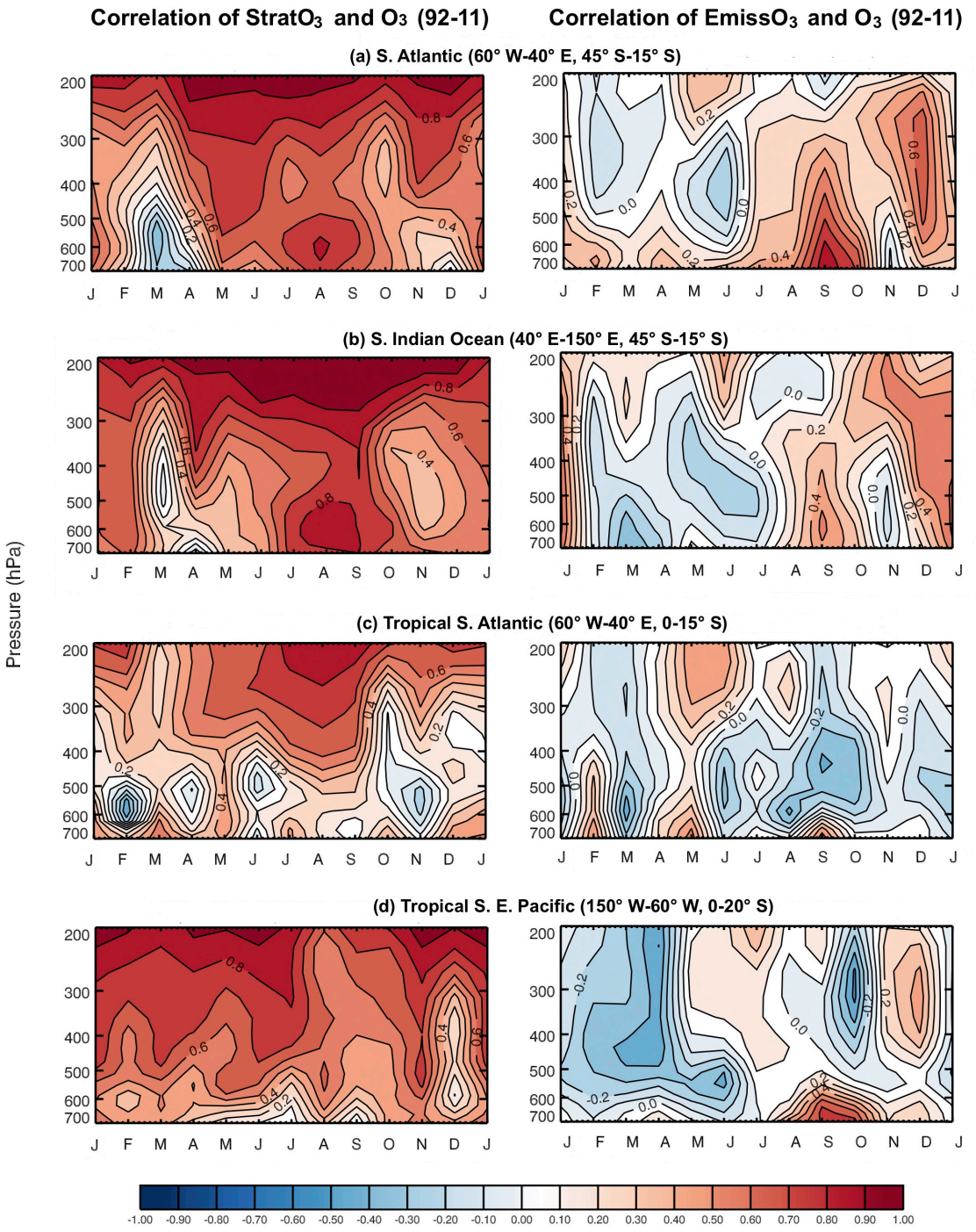

Figure 6: Monthly profile maps of correlations coefficients between ozone and left) $StratO_3$, right) $EmissO_3$ from 1992 to 2011 over (a) South Atlantic (60° W-40° E, 15° S-45° S); (b) South Indian Ocean (40° E-150° E, 15° S-45° S); c) Tropical South Atlantic region (60° W-40° E, 0-15° S); d) Tropical southeastern Pacific (150° W-60° W, 0-20° S). Y-axis is pressure in unit hPa.

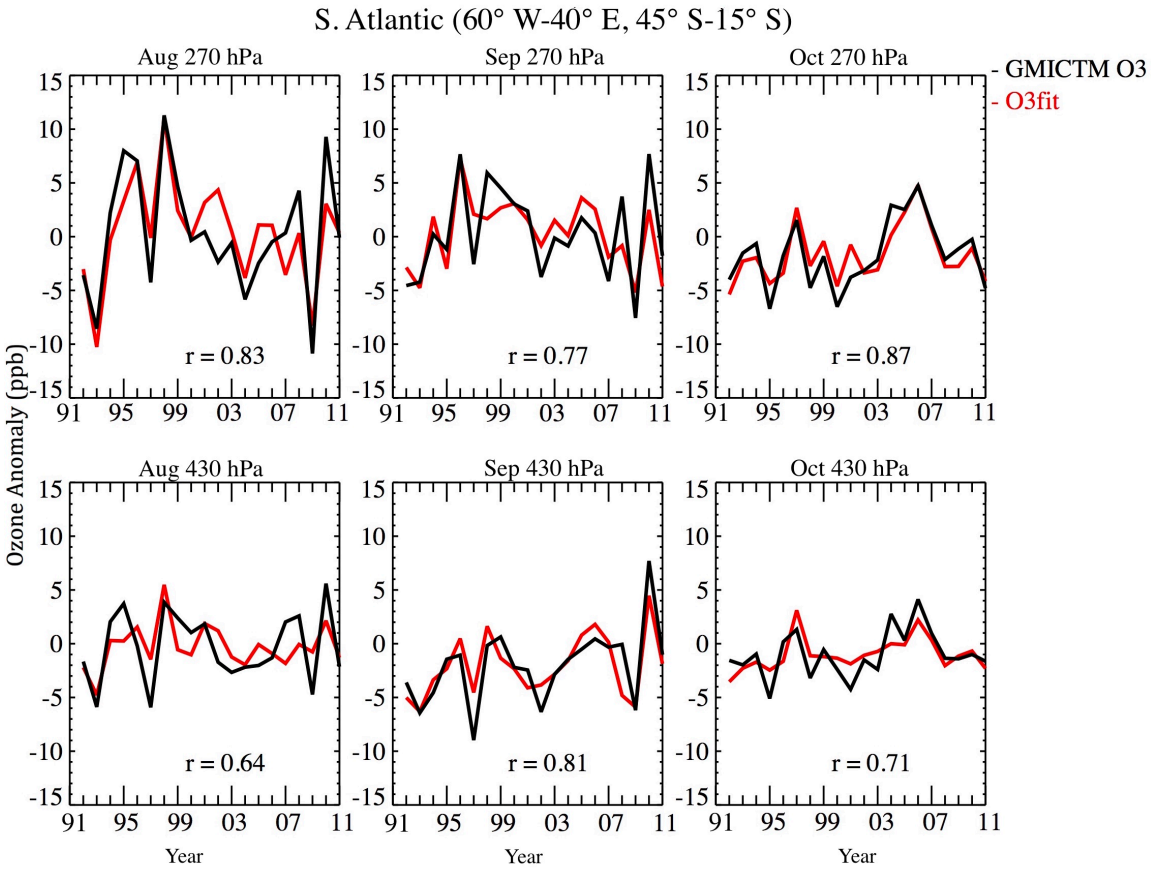

Figure 7: Comparison of the simulated ozone anomalies and the calculated ozone anomalies relying on two predictor variables: $StratO_3$, $EmissO_3$ at 270 hPa and 430 hPa over South Atlantic region. Three panels show results from August (left), September (middle) and December (right) from 1992 to 2011. Unit for y-axis is ppb.

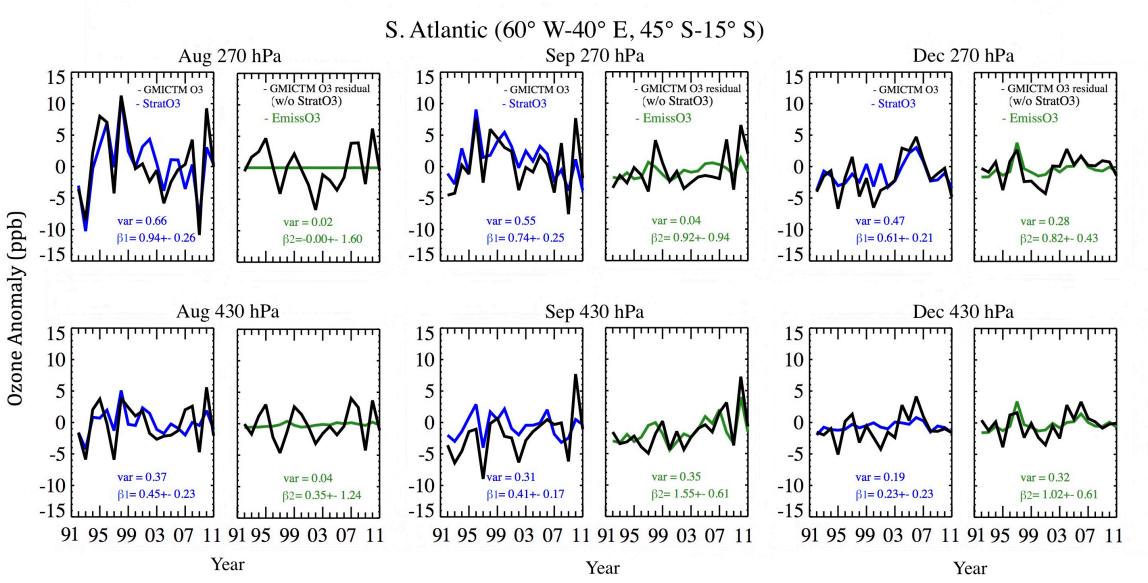

Figure 8: The multi-regression results of simulated ozone anomalies over South Atlantic region relying on two predictor variables: $StratO_3$ (blue), $EmissO_3$ (green) at 270 hPa and 430 hPa. Three panels show results from August (left), September (middle) and December (right) from 1992 to 2011. Each panel contains two columns. The left column of each panel compares the anomalies of $StratO_3$ (blue) and simulated ozone mixing ratio (black) from the GMI-CTM model at 270 and 430 hPa. The right column compares the simulated O_3 residual after removing the regression from $StratO_3$ (black line) and $EmissO_3$ (green line) at these two levels. $EmissO_3$ is calculated from the difference of simulated ozone between the run with yearly-varied emission and the run with constant emission. Unit for y-axis is ppb. The variance explained by each predictor (var), regression coefficient (β) and its 95% confidence level are labeled in each panel.

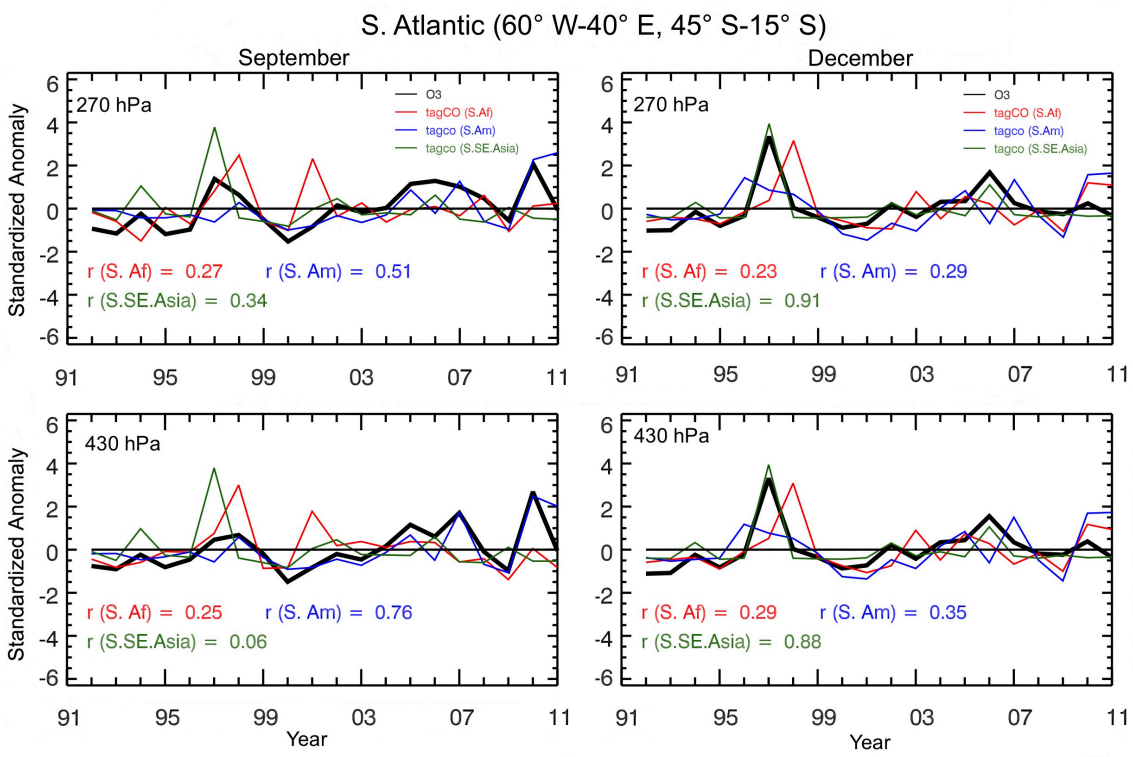

980

981 **Figure 9:** The standardized anomalies of the tagged CO tracers over South Atlantic from
982 three burning source regions, including southern Africa (red), South America (blue) and
983 South and Southeast Asia (green) and their comparison with the EmissO_3 (black) at 270
984 and 430 hPa in September and December from 1992 to 2011.

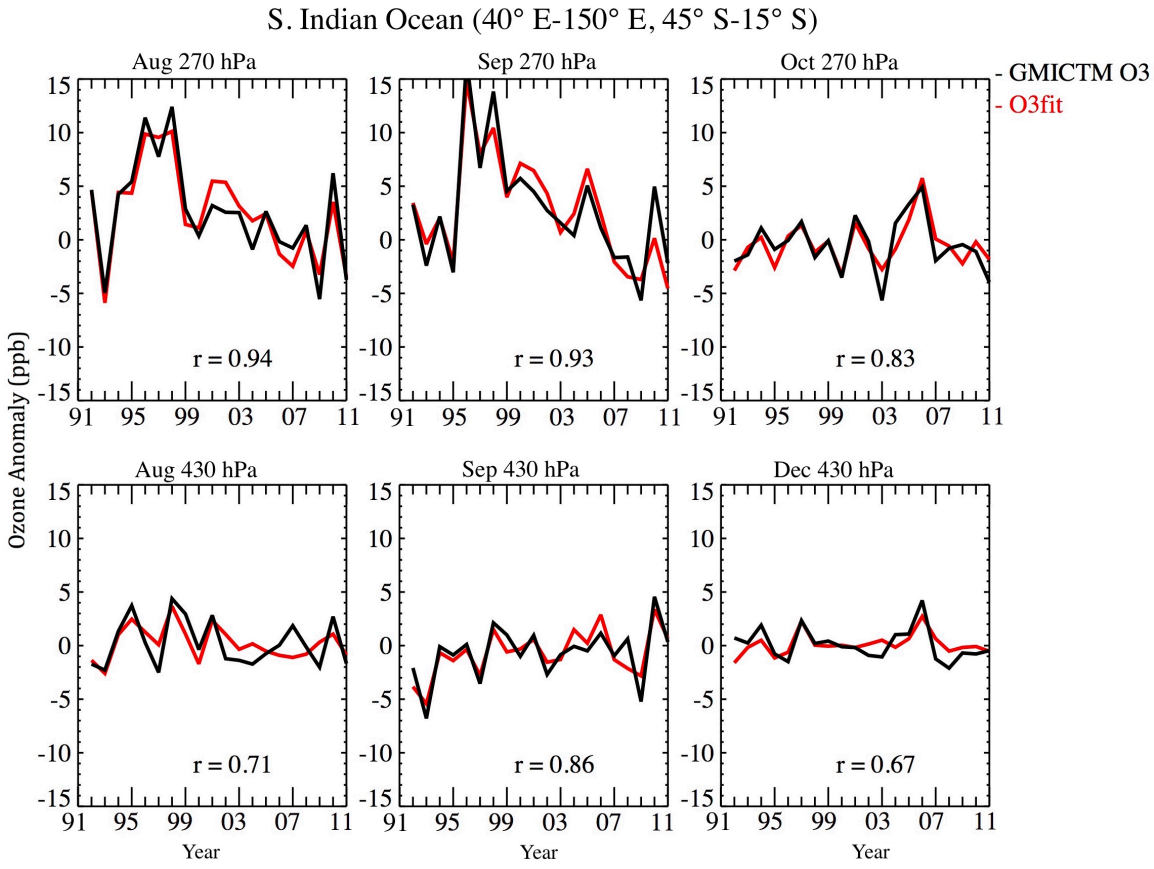

Figure 10: Comparison of the simulated ozone anomalies and the reconstructed ozone anomalies relying on two predictor variables: $StratO_3$, $EmissO_3$ at 270 hPa and 430 hPa over South Indian Ocean region. Three panels show results from August (left), September (middle) and December (right) from 1992 to 2011. Unit for y-axis is ppb.

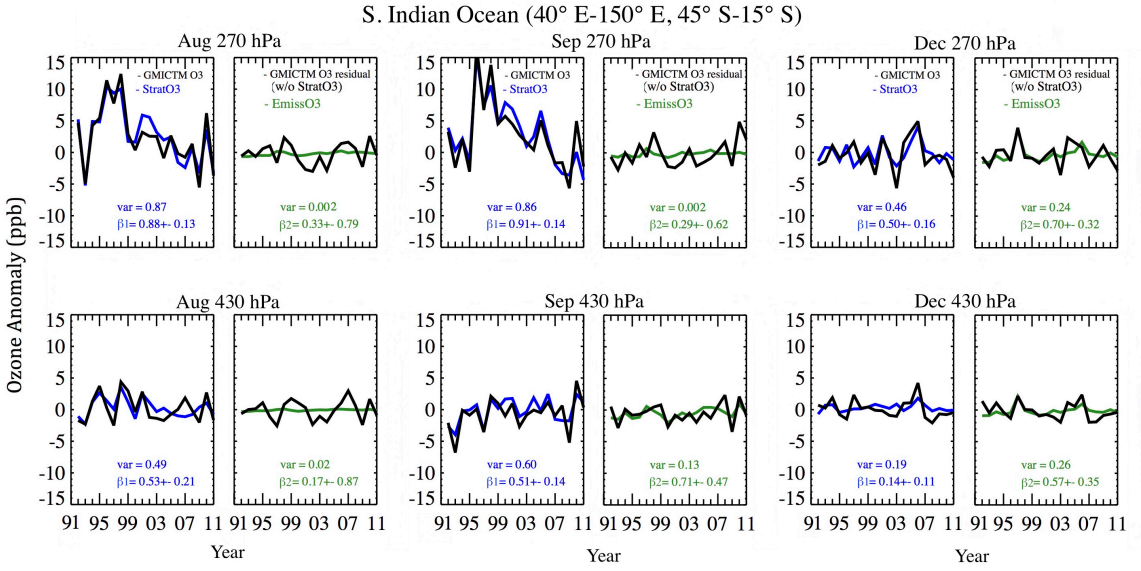

Figure 11: The multi-regression results of simulated ozone anomalies over South Indian Ocean region relying on two predictor variables: $StratO_3$ (blue), $EmissO_3$ (green) at 270 hPa and 430 hPa. Three panels show results from August (left), September (middle) and December (right) from 1992 to 2011. Each panel contains two columns. The left column of each panel compares the anomalies of $StratO_3$ (blue) and simulated ozone mixing ratio (black) from the GMI-CTM model at 270 and 430 hPa. The right column compares the simulated O_3 residual after removing the regression from $StratO_3$ (black line) and $EmissO_3$ (green line) at these two levels. $EmissO_3$ is calculated from the difference of simulated ozone between the run with yearly-varied emission and the run with constant emission. Unit for y-axis is ppb. The variance explained by each predictor (var), regression coefficient (β) and its 95% confidence level are labeled in each panel.

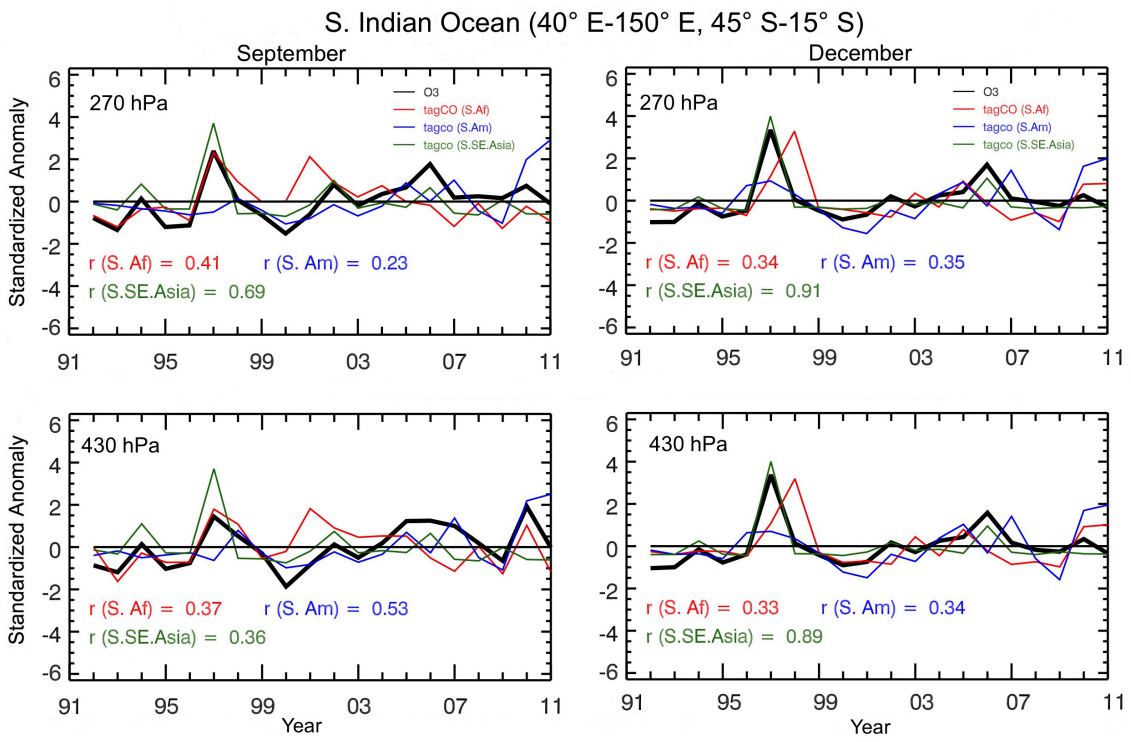

1002

1003 **Figure 12:** The standardized anomalies of the tagged CO tracers over South Indian
1004 Ocean region from three burning source regions, including southern Africa (red), South
1005 America (blue) and South and Southeast Asia (green) and their comparison with the
1006 EmissO_3 (black) at 270 and 430 hPa in September and December from 1992 to 2011.

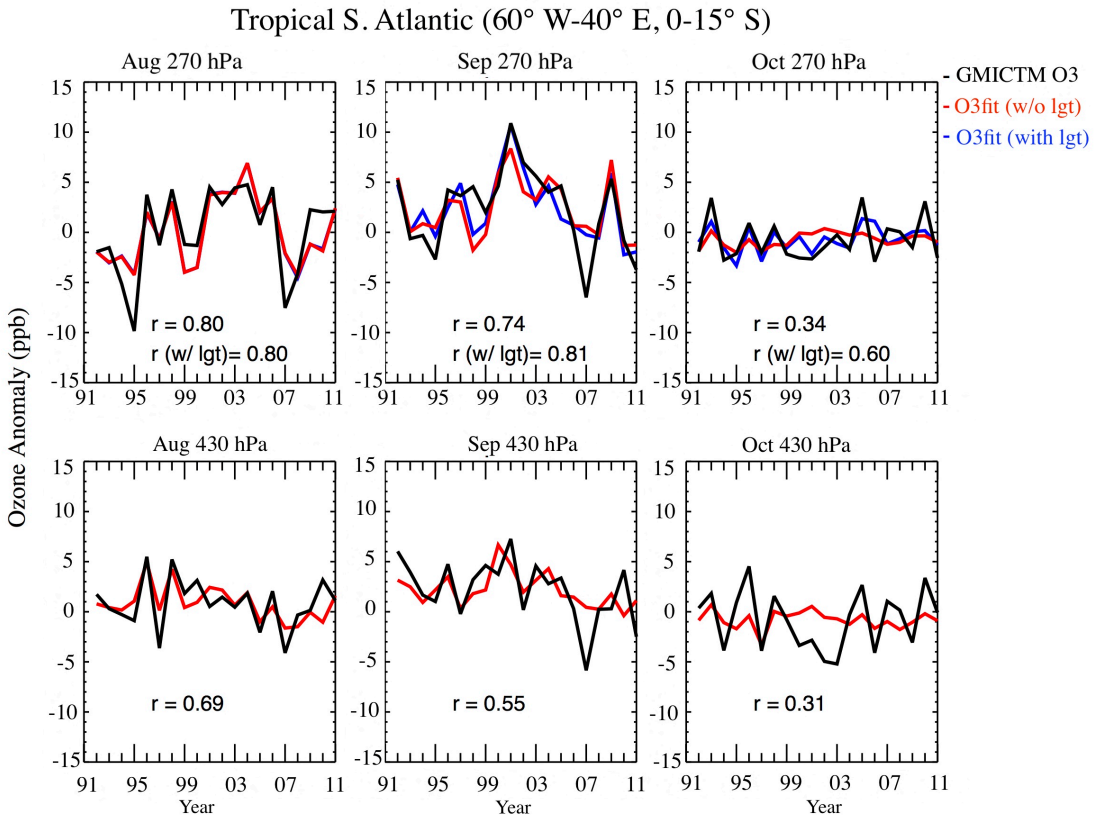

Figure 13: Comparison of the simulated ozone anomalies and the reconstructed ozone anomalies relying on two predictor variables: $StratO_3$, $EmissO_3$ (red) over Tropical South Atlantic region at 270 hPa and 430 hPa. At 270 hPa, the reconstructed ozone anomalies from three predictor variables including lightning NO_X (blue) are added. Three panels show results from August (left), September (middle) and December (right) from 1992 to 2011. Unit for y-axis is ppb.

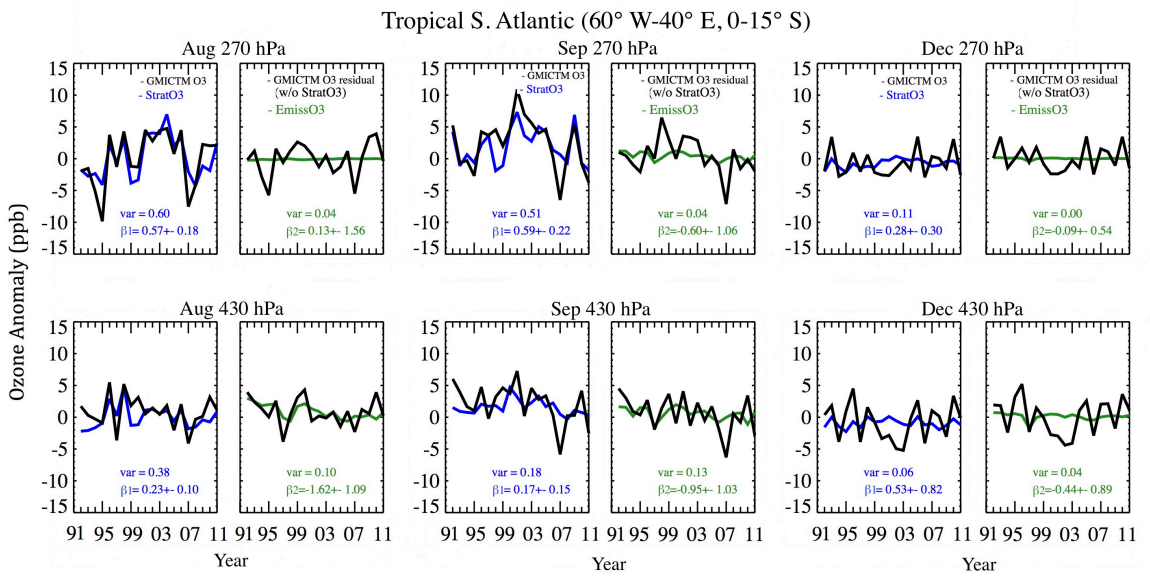

Figure 14: The multi-regression results of simulated ozone anomalies over tropical South Atlantic region relying on $StratO_3$ (blue), $EmissO_3$ (green) at 270 hPa and 430 hPa. Three panels show results from August (left), September (middle) and December (right) from 1992 to 2011. Each panel contains two columns. The left column of each panel compares the anomalies of $StratO_3$ (blue) and simulated ozone mixing ratio (black) from the GMI-CTM model at 270 and 430 hPa. The right column compares the simulated O_3 residual after removing the regression from $StratO_3$ (black line) and $EmissO_3$ (green line) at these two levels. $EmissO_3$ is calculated from the difference of simulated ozone between the run with yearly-varied emission and the run with constant emission. Unit for y-axis is ppb. The variance explained by each predictor (var), regression coefficient (β) and its 95% confidence level are labeled in each panel.

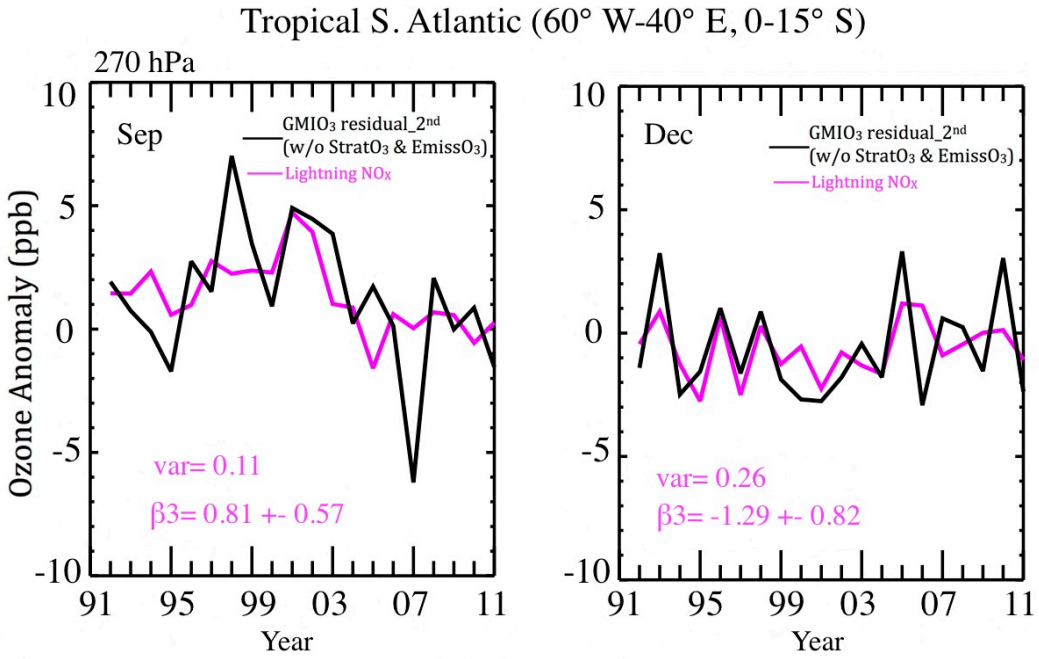

1026

1027 **Figure 15:** The comparison between regression of lightning NO_X (magenta) and the
1028 ozone residual after removing the regression of StratO3 and $EmissO_3$ (black) at 270 hPa
1029 in September (left) and December (right) over tropical South Atlantic region. The
1030 increased variance explained by the regression by adding lightning NO_X (var), regression
1031 coefficient (β) and its 95% confidence level are labeled in each panel.

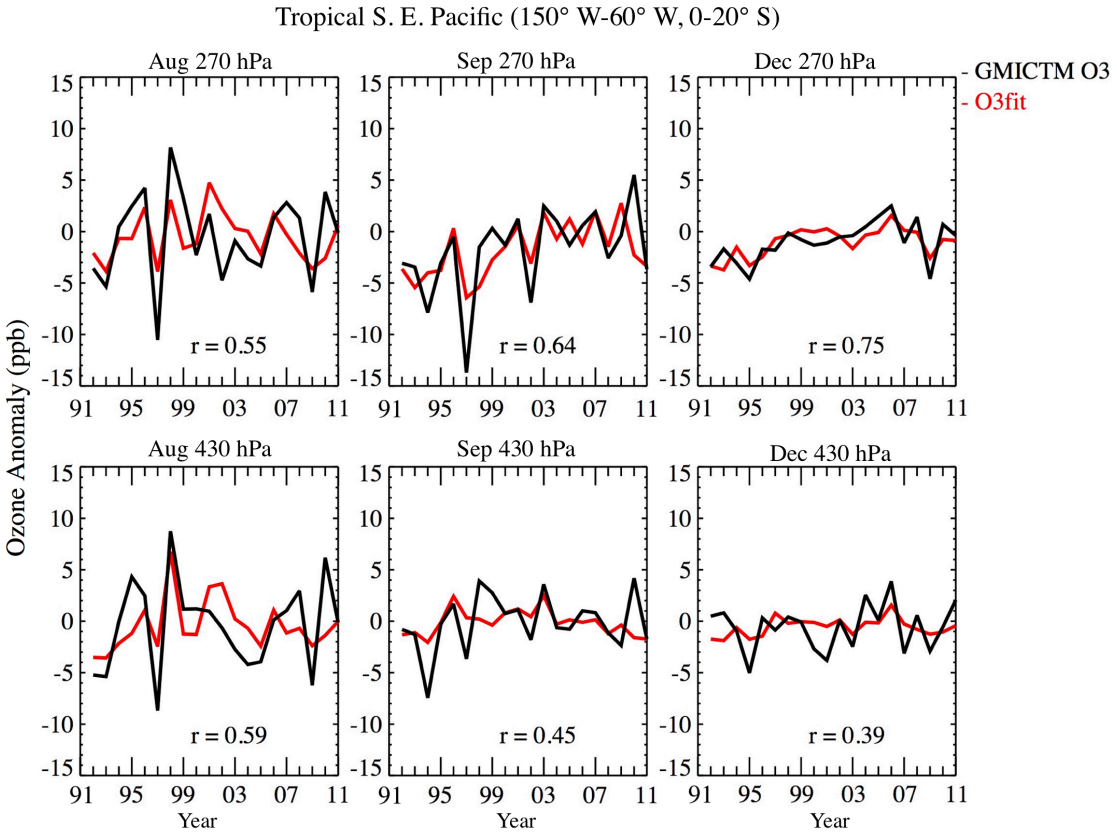

1032

1033 **Figure 16:** Comparison of the simulated ozone anomalies and the reconstructed ozone
1034 anomalies relying on two predictor variables: $StratO_3$, $EmissO_3$ at 270 hPa and 430 hPa
1035 over Tropical southeastern Pacific. Three panels show results from August (left),
1036 September (middle) and December (right) from 1992 to 2011. Unit for y-axis is ppb.

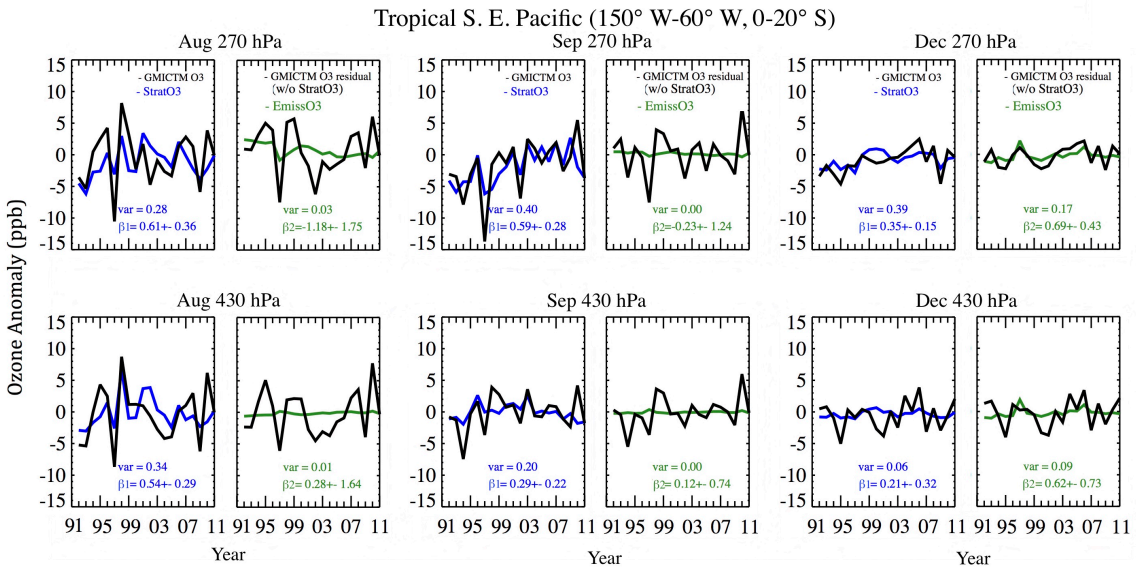

1037

1038 **Figure 17:** The multi-regression results of simulated ozone anomalies over tropical
1039 southeastern Pacific region relying on two predictor variables: $StratO_3$ (blue), $EmissO_3$
1040 (green) at 270 hPa and 430 hPa. Three panels show results from August (left), September
1041 (middle) and December (right) from 1992 to 2011. Each panel contains two columns. The
1042 left column of each panel compares the anomalies of $StratO_3$ (blue) and simulated ozone
1043 mixing ratio (black) from the GMI-CTM model at 270 and 430 hPa. The right column
1044 compares the simulated O_3 residual after removing the regression from $StratO_3$ (black
1045 line) and $EmissO_3$ (green line) at these two levels. $EmissO_3$ is calculated from the
1046 difference of simulated ozone between the run with yearly-varied emission and the run
1047 with constant emission. Unit for y-axis is ppb. The variance explained by each predictor
1048 (var), regression coefficient (β) and its 95% confidence level are labeled in each panel.

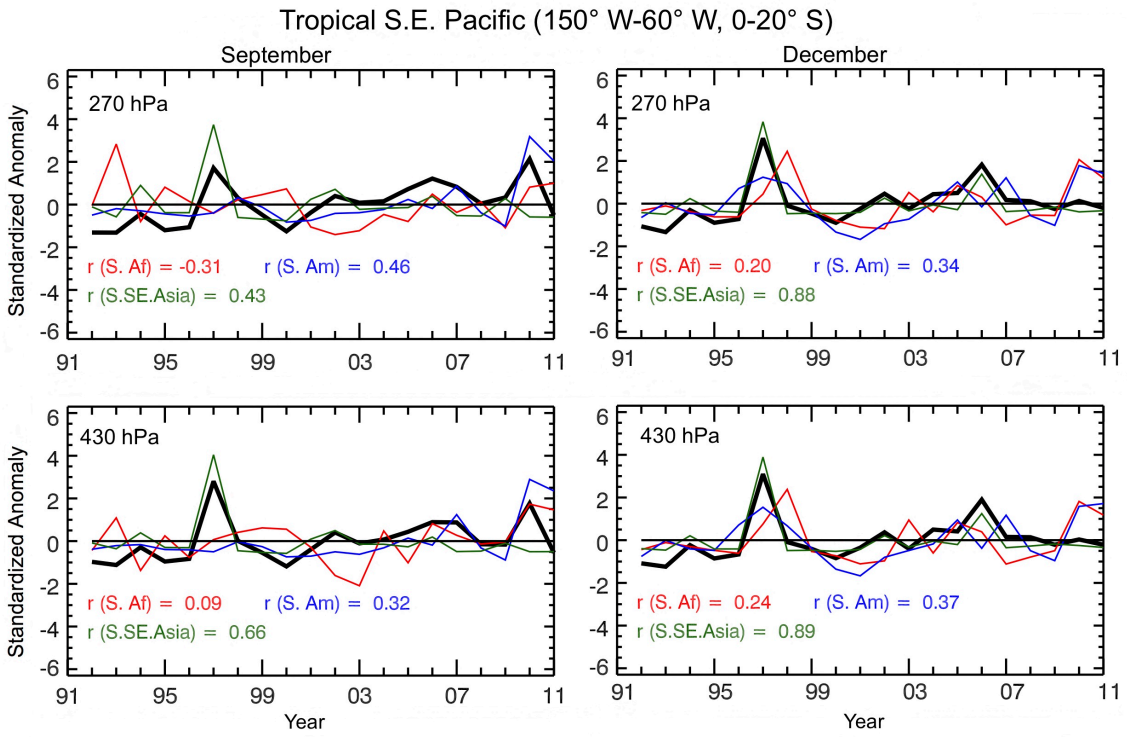

Figure 18: The standardized anomalies of the tagged CO tracers over tropical southeastern Pacific region from three burning regions, including southern Africa (red), South America (blue) and South and Southeast Asia (green) and their comparison with the EmissO3 (black) at 270 and 430 hPa in September and December from 1992 to 2011.

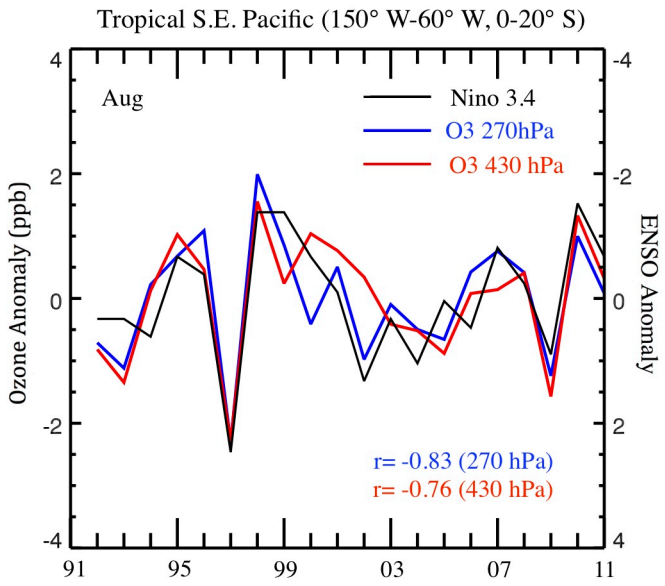

Figure 19: Comparison of IAV of ozone anomalies over tropical southeastern Pacific region at 270 hPa (blue) and 430 hPa (red) with Niño 3.4 index in August from 1992 to 2011. The 2nd y-axis for the ENSO anomaly is reversed.